IAS SEDIMENTOLOGY
Journal of the International Association of Sedimentologists

Shark fins: overturned flame patterns due to waves at the shear horizon of a flow-bed boundary. Examples from the 2006 pyroclastic currents deposits at Tungurahua

Journal:	*Sedimentology*
Manuscript ID	Draft
Manuscript Type:	Original Manuscript
Date Submitted by the Author:	n/a
Complete List of Authors:	Douillet, Guilhem; Universität Bern, Institut für Geologie; Ludwig-Maximilians-Universität, Department für Geo und Umweltwissenschaften Chaffaut, Quentin; Universite de Strasbourg Ecole et Observatoire des Sciences de la Terre Schlunegger, Fritz; University of Bern, Institute of Geological Sciences Kueppers, Ulrich; Ludwig-Maximilians-Universität, Department für Geo und Umweltwissenschaften Dingwell, Donald; Ludwig-Maximilians-Universität, Department für Geo und Umweltwissenschaften
Keywords:	shark-fin, convolute laminae, flame structures, overturned beds, flow shearing, pyroclastic currents

Shark-fin structures: overturned convolute and flame patterns due to waves at the shear horizon of a flow-bed boundary. Examples from the deposits of the 2006 pyroclastic currents at Tungurahua volcano (Ecuador)

Guilhem Amin Douillet[1,2], Quentin Chaffaut[2, 3], Fritz Schlunegger[1], Ulrich Kueppers[2], Donald B Dingwell[2]

[2] *Institut für Geologie, Universität Bern, Switzerland*

[2] *Ludwig-Maximilians-Universität München, Germany*

[3] *Ecole et Observatoire des Sciences de la Terre, Strasbourg, France*

Keywords: 1. shark-fins, 2. convolute laminae, 3. flame structures, 4. overturned beds, 5. flow shearing, 6. pyroclastic currents

Running title: Overturned "shark-fins" in deposits of pyroclastic currents

Abstract

Enigmatic structures are documented in deposits of dilute pyroclastic currents and grouped under the term "shark-fins". They consist of an overturning of a few laminae on a decimeter scale, forming overbent "flames" or convolute laminae, which occur in successive, periodic patterns. More than 200 shark-fins were investigated and measured in the cross-laminated deposits from the 2006 pyroclastic currents of Tungurahua volcano (Ecuador).

These shark-fins are interpreted in terms of syndepositional soft sediment deformation pattern whereby waves form at the interface of a shear horizon at the flow-bed boundary and rework the bed. The shark-fins are not related to Kelvin-Helmholtz instabilities. Instead, a theoretical framework based on two layers separated by a shear horizon is developed. The calculated growth rate of the waves is compared to sedimentation rates in order to infer aspects of the stability and preservation of such sheared interfaces. The process-based interpretation is supported by the results from the physical model.

Various other incidental patterns are presented and discussed, which likely result from collisions of flows with deposits, intraflow events and syn-flow slumping. We thus identify the necessary key observations for the interpretation of shark-fin structures for different types of triggers. Such observations on flow-bed interactions contribute to the understanding of a flow rheology, shear partitioning, and the transmission of shear stress out of the flow and into the substrate.

1. Introduction

1.1. Pyroclastic currents

Pyroclastic currents are flowing mixtures of gas and particles ejected during explosive volcanic eruptions (e.g. Branney and Kokelaar 2002, Dufek 2016, Palladino 2017). From the analysis of deposits, a transitional span of flow transport processes has been postulated ranging between two end-member behaviors: granular flow type and fully turbulent, gas-dominated current (e.g. Sparks 1976, Fisher 1979, Douillet et al. 2013a). The high particle-concentration end-member behavior (granular flow type) is typically inferred from massive, unsorted, coarse-grained (m-size boulders) deposits, which are attributed to pyroclastic currents, where sediment transport is accomplished through a dense granular flow dominated by particle interactions (e.g. Lube et al. 2007, Bernard et al. 2014). The low particle-concentration end-member (turbulent flow type) is inferred from sediments organized as cross-laminated bedsets forming dune bedforms, generally finer and better sorted in terms of grain-size distribution (e.g. Walker 1984, Cole 1991, Douillet et al. 2013a, 2013b). The depositional areas are generally organized as marginal and localized patches on the outer overbanks of pathways of the main pyroclastic current (e.g. Douillet et al. 2013a and references therein). For those, the transport mechanisms are interpreted as related to fully "dilute" pyroclastic currents with a relatively low particle concentration where the dynamics are largely dominated by fluid turbulence (gas, e.g. Wohletz and Sheridan 1979, Branney and Kokelaar 2002, Douillet et al. 2013b, Dellino et al. 2014).

A continuous spectrum of deposit types is observed so that the boundary between these two end-members seems diffuse. Sedimentological analyses are further complicated by the fact that the deposits mainly reflect the influence of variations at the flow-bed boundary layer (Branney and Kokelaar 2002, Douillet et al. this issue). These deposit-based models have been validated and refined through theoretical, analogue and numerical models (Sulpizio et al. 2014, Dufek and Bergantz 2007, Esposti-Ongaro et al. 2008, 2011), which highlight the interplay and coupling between dense underflows and overriding turbulent currents (Burgisser and Bergantz 2002, Breard et al 2016, Breard and Lube 2017). Where transport is supposed turbulent (dilute pyroclastic currents), such flows are thought to resemble the characteristics of subaqueous turbidity currents. Indeed, in contrast with traditional aeolian and river sediment transport, dilute pyroclastic currents likely behave as particulate density currents (Kneller and Branney 2000). Particulate density currents receive their momentum through their larger density compared to the ambient fluid. Their particularity is that the agent carrying this excess density are the transported particles. The same particles that drive momentum during transport thus also constitute the sedimenting load that deposits when momentum decreases. Finally, in a particulate density current, the particles are distributed over the whole height of the current rather than being eroded and transported near the bed only (e.g. Douillet et al. 2014). These subtleties make the dynamics of transport and deposition of particulate density currents unique.

Here, intriguing structures grouped under the term "shark-fins" are documented. They consist of a few overturned laminae over a decimeter scale extent, and occur as successive, periodic patterns on the lee side of dune bedforms. These overbent "flames" and convolute laminae are observed in sediments from the pyroclastic currents related to the 2006 eruption of Tungurahua volcano (Ecuador). The shark-fins were discovered after impregnating the outcrops with epoxy resin thereby producing sediment plates (lacquer peels), which enabled to observe the lamination at a highly detailed resolution (Douillet et al. submitted-a, in sub.-b). Although sparsely reported, such shark-fins have never been systematically investigated. We believe that they are likely to be common in many more settings. Under the assumption that a flow is a closed system that primarily interacts and exchanges energy between its basal part and the bed (and to some extent, at the upper free boundary with the ambient fluid), syndepositional overturned patterns can yield valuable information on the dynamics and rheology of the parental currents.

1.2. Soft sediment deformation at the flow substrate boundary

Geological outcrops exhibiting convolutions or patterns associated with the deformation of sediment stratae have been recognized for more than 150 years (Logan 1863, Allen 1982 pp. 343-393, Maltman 1994 and references therein). The processes of soft sediment deformation (SSD) are understood as the deformation of sediment beds before their consolidation (see review by Shanmugan 2017). They are generally interpreted to occur when a granular bed acquires a transient property of a liquid, either due to shaking -i.e. liquefaction- or due to an upward movement of the interstitial fluid -i.e. fluidization- (e.g. Lowe 1976, Nichols et al. 2010). The triggers that have been postulated for SSD include seismogenic shaking, post-depositional gravity transport (slumping), fluid escapes, loading (Owen et al. 2011), and tsunamis (e.g. Matsumoto et al. 2008). In pyroclastic deposits, other types of SSD structures and triggers have been invoked, such as ballistic impacts, deformation by pressure waves produced by eruptive explosions, post depositional deflation of a fluidized flow, or basal shear from a granular-based flow (Douillet et al. 2015).

1.2.1. Overturned beds

"Conventional overturned beds":

"Conventional overturned beds" are defined here as patterns in sediment beds where (i) the stratal organization indicates that the top part of the bed was slightly translated with an orientation toward the downstream direction, and where (ii) laterally coherent structures involve a large amount of laminae over a length much greater than the thickness of the deformation and (iii) the boundaries of the bedsets are planar and unaffected by the deformation. Whereas most authors agree that these features are formed in relation to a current, various processes have been suggested for the specific mechanisms, such as the pure shear of the flow, the scraping of logs and debris transported by a current, or a combined effect of earthquake-induced liquefaction as a current shears the bed.(Allen and Banks 1972 and references therein). Recent results from analogue experiments have shown that the velocity profile of a laminar flow doesn't vanish at the flow-bed boundary if monitored for long enough, but penetrates into it on a short diffusion thickness (Houssais et al. 2015). This suggests the occurrence of a shear component partitioned out of the flow.

"Shark-fin structures":

"Shark-fins" are defined here as a generic term to refer to a different type of overturned structures (Fig 1-4). These share many of the characteristics of conventional overturned beds (see above), but they occur as laterally very confined and narrow structures, involving only a few laminae, and are often found in trains of several structures. Further, the upper limit of these overturned beds is not planar, but rather forms a positive topographic anomaly. Several types of structures fall in the group of shark-fin patterns and have commonly been described as "flow oriented convolute beds", "flames" (Butler and Tavarnelli 2006), "truncated flame structures" (Matsumoto et al. 2008), "imbricated flame structures and pseudonodules" (Larsen 1989), "asymmetric flame structures" (Butler et al. 2015), "tightly folded overturned anticlines and synclines" (Crowe and Fisher 1973). shark-fin patterns have been reproduced in particular in the grounding experiments by McKee et al. (1962a, 1962b) by "crinkling" laminated beds through different techniques: slumping, vertical loading, but also dragging sand bags across the surface or forcing very strong currents at the bed interface.

Here, shark-fins are described based on natural deposits from the 2006 pyroclastic currents at Tungurahua volcano (Ecuador). We discuss their origin in terms of physical processes, provide quantitative measurements of > 220 of these structures, and develop a theoretical framework for their analysis.

1.2.2 Wavy shear patterns at the flow-bed boundary of experimental sediment gravity flows

The question of how granular flows interact with the erodible substrate upon which they flow has been studied in various contexts. In addition to the theories on the formation of conventional overturned beds, recent research has demonstrated that local wavy patterns and shear instabilities can develop at the interface between a flow and its substrate. These phenomenas can have crucial effects on the dynamics and rheological parameters of a flow.

In this context, a fundamental study on wave instabilities in a granular medium was carried out by Goldfarb et al. (2002), who reported that “breaking waves” (i.e. vortical, repetitive in-train wave instabilities) could form at the vertical interface between two streams of identical grains. They suggested that the competing shear and extensional strains produced such instabilities. Rowley et al. (2011) produced vortical patterns preserved in deposits where a decelerating granular flow passes over a stratified substrate of similar grains. These structures have been observed on vertical transects, and thus a gravitational component in the force balance may be present whereby the vortical shapes may suggest a rotational component linked to buoyancy. Further, the vortices occurred in trains of several repetitions, suggesting their formation through an oscillatory (wave) mechanism. Although pointing out the differences inherent in the physics of granular flows, the authors compared the vortical patterns with Kelvin-Helmholtz instabilities occurring in pseudo-Newtonian fluids.

For the case of subaqueous environments, Verhagen et al. (2013) launched a series of studies on the interaction of subaqueous sediment gravity flows with their substrate. They released clay-laden, bottom-hugging density currents over a lowly packed, “fluidized” bed of clay, and showed that these could interact and form “interfacial waves” at the flow-bed boundary, “leading waves” ahead of the front of the current, or induce "chaotic mixing" with the substrate. They noted a dependency on the stability field of each type of interaction with the dimensionless Richardson number, without explicitly mentioning gravity waves or Kelvin-Helmholtz instabilities. In a similar setting focused on subaerial lock-exchange granular flows, Roche et al. (2013) showed that “the sliding head of a granular flow generates a dynamic upward pore-pressure gradient at the flow-substrate interface. The associated upward air flux was enough to fluidize a substrate of fines, so that particles were not entrained individually but the substrate instead [was] subject[ed] to small shear instabilities”. Using the same setup, Farin et al. (2014) refined the observation, noting that granular flows formed “waves made of particles excavated from the erodible bed at the flow head” and that their maximum amplitude increased with the aspect ratio and volume of the released flow. They also compared these waves with Kelvin-

Helmholtz instabilities. Most recently, Pollock et al. (2017) experimentally triggered the growth of in-train, repetitive wave-like features along the interface between a high pore-pressure granular flow in a frictional regime. These authors were able to vary the scale of these features as a function of the fluidization state.

1.2.3. Shear structures and overturned beds in natural turbidites

A variety of shear structures have been attributed to flow shearing in deposits of turbidity currents (in the broad sense of subaqueous particulate density currents). Early workers noted for deformed turbidite beds that "convolutions are a fossil record of the forces which operated upon laminated bed during its sedimentation" (Dzulynski Smith 1963). Larsen (1986) interpreted that "oblique flames and pseudo-nodules" resulted from shearing of loosely packed deposits caused by the still moving turbidity currents. Butler and Tavarnelli (2006) postulated a deformation during the emplacement phase from the interpretation of a combination of flow-aligned mud injections, boudinage and sheared flames. Postma et al (2009, 2014) identified flame structures elongated/overturned in the paleoflow direction at the border of steeply truncated beds. They compared these structures to footages of a series of analogue experiments on hydraulic jumps within turbidity currents, where reworking of the bed was triggered by variations in the intensity of the hydraulic jump in its "pool". "Substrate wings" from detachment, convolute laminations, sills and dikes were documented at the base of turbidite beds and linked with erosion steps from these flow (Eggenhuisen et al. 2011). Eye and sheat folds, occurring in intervals of 2-10 cm thickness together with convolute laminations have tentatively been related to the syndepositional shear strain from turbidity currents acting on an aggrading ripple bed substrate (McClelland et al. 2011, Marques 2012). Several classification schemes and criteria have been proposed to figure out the exact timing and processes of syndepositional shearing and also suggest a density-driven Kelvin-Helmholtz mechanism (Butler et al. 2015, Gladstone et al. 2017).

1.2.4. Intraflow beds and bulldozer effects

Building on the analogue experiments of Verhagen et al. (2013), Baas et al. (2014, 2016) enlarged the fields of flow-bed interactions and showed that "the lower part of turbidity currents has the ability to enter fluid mud substrates". They conclude that such "intrabed currents are driven by bed shear stress exceeding the bed cohesive strength, and by flow density exceeding bed density". The resulting deposits showed various soft sediment deformation patterns such as scour fills, load and fluid escape features, flame structures and bed derived "plumes" in the overlying beds. Using polydisperse granular mixtures in pyroclastic current analogue experiments, Sulpizio et al. (2017) showed the entrapment of loose material from the substrate when the flow passed over the bed, with a rotational component attributed to high shear stress at the flow-bed boundary. Their experiments seem to produce single structures at the onset of the affected deposits, without the occurrence of recurrent oscillations or wavy in-train patterns. At a different time-scale of flow-bed interactions, Morgenthaler and Frehner (2017) provided evidence that a bulge can form at the front of a creeping rock-glacier and interpreted it as due to a "frontal bulldozer-like soil erosion" effect. Whereas the densities and the timescales of these periglacial deposits are largely different to the frontal waves of turbidity currents (Verhagen et al., 2013) or overturning due to dry granular flows (Sulpizio et al., 2017), the resulting structures share similarities and the processes might be comparable.

1.2.5 Existing field evidence in deposits of pyroclastic currents

The influence of shearing of a pyroclastic current on its aggrading substrate was evidenced through various sedimentary indicators. Crowe and Fisher (1973) were the first to note that "tightly folded overturned anticlines and synclines" "showed the evidence of the influence of the currents on their origin" at Ubehebe (California). Without explicitly mentioning overturned structures, Fisher (1990) recognized at Mt St. Helens (Washington) that finger-like dikes of tephra intruded in the unconsolidated substrate. He suggested that the flow head plowed into the soil and mixed it, and further that the structures may have been "caused by vortical motion, rotating material from within the head of the blast surge to the ground surface during erosion of the furrow". Cole et al. (1993) proposed that gradings of breccia/lithic concentrations at Roccamonfina (Italy) were related to "internal shear producing overriding or overlapping of the rear of the flow onto the slower-moving front part". Reverse faults (ca. 30-60 cm long) that offset the basal contact of an ignimbrite at Monte Cimino (Italy) were interpreted as syn-depositional substrate deformation due to the shear of the pyroclastic current (Laberge et al. 2006). Pajeras et al. (2010) documented outcrops from Villa Rica (Chile) described as "folded, sheared, and thrust-faulted along the contact" -see their Fig. 9- that definitely fall in the definition of shark-fins. They also noted that "subtle erosion and amalgamation surfaces [...] showed that the pulsatory flows were able to remobilize ignimbrite laid down earlier during the same eruptive phase". Meter-scale features from the Poris ignimbrite (Teneriffa) and some small-scale flame structures from the Tanjung formation (Indonesia) were related to syn-flow shear instabilities by Rowley (2010). Douillet et al. (2015) documented small-scale shark-fin patterns in relatively massive units from the Ubehebe crater (California) and additionally identified the signature of the migration of shark-fins in examples from the 2006 deposits of Tungurahua. Following Rowley et al (2011), they interpreted these as structures that would result from the freezing of granular Kelvin-Helmholtz instabilities. From a theoretical analysis, Douillet et al. (2015) suggested that such instabilities would develop for relatively slow-moving mixtures (generally below 0.5 m/s). Recently, Brand et al. (2017, figure 10) and Pollock et al. (2017) recognized large-scale patterns similar to shark-fins in the deposits of the 1980 pyroclastic currents of Mt. St. Helens (Washington). They seem to have occurred when the main flow interacted with localized lenses of material from a previous flow.

2. Data

2.1. A dataset based on the 2006 eruption of Tungurahua

The structures reported here are preserved in the deposits from the 17 August 2006 eruption of Tungurahua volcano (Ecuador). This eruption triggered the formation of pyroclastic currents that were funneled in ravines of the fluvial drainage network on the steep flanks of the volcano (e.g. Kelfoun et al. 2009, Douillet et al. 2013a, 2013b, Rader et al. 2014, Bernard et al. 2014, Benage et al. 2014, 2016). Cross-laminated sediments forming dune bedforms dominated by ash are preserved as marginal, isolated patches with an extent of several hundreds of meters on the overbanks of the ravines that directed the flows (Douillet et al. 2013a, 2013b). These dune bedforms have been grouped into four end-members according to their shapes: "elongate", "transverse", "lunate", and "2D". For each bedform type, a set of sediment plates (lacquer peels) has been produced in order to capture the highest level of details about the sedimentary structures (Douillet et al. in-sub-b).

All shark-fin structures documented here were evidenced in these cross-laminated dune bedforms and co-exist within bedsets including (Fig 5, Douillet et al. 2013b, this issue):

- (i) a general stoss-depositional tendency,
- (ii) sub-vertical to horizontal truncations of stoss-faces,
- (iii) planar laminasets evolving into stoss-aggrading ripples,
- (iv) partial to total absence of stratification (diffuse to massive aspect) in some beds, laterally evolving into diffusely laminated beds, and
- (v) a dominance of planar lamination on the lee of crests.

It is worth emphasizing at this stage that no water was involved in the flow of the pyroclastic currents.

A set of four sediment plates from four different bedforms and two sets of four parallel sediment plates from two other bedforms were screened (Fig 1-5). They represent the entire range of shape types identified in Douillet et al. (2013b). Each sediment plate has a length of 3 m aligned with the flow direction, and heights varying between 0.8 and 1.8 m, thus representing ca. 43 m^2 of outcrop. Deformation patterns were absent in two dominantly massive and coarse-grained bedforms (lapilli / gravel sizes dominated), but present in all fine-grained outcrops (ash / sand size range).

2.2. Description and classification:

The shark-fin patterns form an overturning of laminae and are,elongated toward the down-flow direction exclusively. They consist of a "tail" which is linked to the laterally adjacent planar laminae via "roots" (Fig 1). Two hundred and twenty three structures were identified, described, measured, and classified. Three different end-members were recognized based on their architecture (Fig 2-4):

- "*convolute shark-fins*" (146 structures, Fig 3): the overturned tail can be followed laterally to non-deformed sets without a truncation of the lamination, so that two roots are present upflow and downflow from the tail. The laminae are fully preserved.
- "*truncated ripple shark-fins*" (64 structures, Fig 4A-D): the patterns are found at the interface of a ripple-sized heap delimited by a truncation of the laminae. Only one root and the overturned tail are present.
- "*flat truncation shark-fins*" (13 structures, Fig 4E): the overturned laminae are found underlying a flat and laterally continuous erosion plane.

The shark-fin patterns are wholly dissimilar to "conventional overturned beds", which include an entire stratal package on a much broader lateral extent (e.g. Allen and Banks 1972, see 1.2.1). A variety of overturned geometries is recognized, spanning the range between smoothly distributed overturning forming bulbous, rounded style tails with a "logarithmic shape" (e.g. Fig 3B) to highly angular tails bent only at localized knickpoints giving a "chevron-like shape" (e.g. Fig 3A, 3D). Note as well that almost no documented features have their tail dipping downward (aligned with the gravity force), and the patterns are only elongated in the downflow direction without vertical re-arrangement.

2.3. Occurrence and spatial recurrence:

Occurrence:

Most shark-fin structures occur on the lee side of bedforms, on a flat or gently dipping palaeo-surface (lamina or erosion) with slope between -5º and 25º (Fig 5, 6A). Shark-fin structures are most common in three types of settings:

- in relation with a low-angle erosion plane (Fig 7A),
- within a zone of disturbed beds (occurring as confined lens or laterally continuous layer) concordant with the dip angle of the lee side of a dune bedform (Fig 7B, 7C base),
- directly at a lamination crest-knickpoint or within a short distance downstream from a bedform's crest (Fig 7C top).

Spatial recurrence:

Within these settings, shark-fin structures are often organized as pairs, triplets or quadruplets and rarely more, independently of their type. The spacing between these groups is generally small (5-50 cm), and the patchy organization can be expressed in two ways:

(i) either along a single horizon with downstream repetitions (i.e. "wavy in-train patterns" concurrent in the same temporal interval, Fig 7).

(ii) Alternatively, several structures are close in locations but occur at different stratigraphic levels, yet generally within the same co-sets (i.e. "climbing in the stratigraphy - spatial stability in time, Fig 8).

Where they occur "in-train" on the same horizon, the length between successive "shark-fins" was systematically measured (Fig 9A). Whereas the inter-structure distances are a priori not correlated, they appear to be arranged as multiple of each others within a single train. Fairly constant patterns become evident upon dividing the separation length by 2 or 3 (which corresponds to plotting the harmonics in the case of a wave, Fig 9B). This suggests that an actual pseudo-wavelength is present, yet not always apparent as some of the shark-fin occurrences are not visible in the deposits. In some cases, those trains can be related to nearby surface irregularities a few tens of cm upstream, being either a scour/gulley at the considered horizon or an accidental small block lying on the bed surface.

In some cases, those trains can be related to nearby surface irregularities, either negative ones as scours or gulleys following local erosion, or positive ones as clasts that have been deposited.

Ploughed zones:

Many of the shark-fins are laterally accompanied by zones that seem substantially disturbed, where lamination is only diffuse and lineations with an angle to the bedsets are visible (Fig 8B-8C). These zones seem to have undergone consequent mixing, and their grain size distribution is less sorted than that in non-disturbed beds. Here, the term "ploughed zones" is used in the description to refer to these thin lenses accompanying shark-fin trains.

2.4. Dimensions

For each encountered shark-fin, a series of parameters were measured (Fig 1): length (the extent of the deformed zone), thickness (from root to top of tail), elongation (the amount of overturning), number of overturned laminae, grain-size and stratal organization of underlying and overlying beds, slope angle of affected beds and affecting contact, lateral continuity (up- and down-stream), distance to the next structure when part of a train, and position within the outcrop (Fig 5).

At Tungurahua, the dimensions of the shark-fins are relatively homogenous (Fig 6, Table Annex 1), and vary by only one order of magnitude between extremes, both in terms of length, thickness, and number of affected laminae (Mean/Max/Min values of 5.68 / 20 / 1.5 cm for lengths, 1.48 / 5 / 0.3 cm for thicknesses and 9.19 / 24 / 3 for affected laminae). Although linear regressions were plotted to highlight trends in the graphs, we do not conclude linear trends for these structures, and the data are quite broadly distributed within the entire dimensional windows (Fig 6). Thicknesses of deformation remain very superficial and never exceed 5 cm. The subgroups of convolute- / truncated-ripple- / flat-truncation- shark-fins differ in trends mainly because convolute shark-fins tend to be thicker for similar lengths/number of involved laminae/elongation. This is expectable since a truncated structure is likely to be less thick than a fully preserved one.

2.5. Anecdotic patterns

Three zones had particular patterns that could not be included in the classification but are described hereafter.

Abnormal disturbed zones:

Whereas most truncations are observed on stoss sides, one transect in the lunate bedform exhibits extremely curious unconformities and deformed patterns deviating from the usual trend (Fig 10). Several zones have an abnormal aspect (pink zones in Fig 10A), consisting of patches with laterally in-train shark-fins, intact planar lamination, massive zones, diffuse, possibly ploughed lenses, and vertically spread shark-fins,. The shark-fins have singular bulbous shapes, yet oriented toward the downward/downflow direction (Fig 10C-E). Enigmatic step-like laminae are also present in the upper part of the zones (Fig 10B). These abnormal zones are >15 cm thick, and can be followed on a length of >2 m. They are initiated on lee sides, directly downstream paleo-crests' knickpoints, and are generally highlighted by a scar forming a basal unconformity or zone with trains of shark-fins (Fig 10B) that gradually becomes conformable with the underlying lamination. Three of these onset-scars are clearly recognized, and their accompanying disturbed zones vanish or become mixed together farther downstream (Fig 10A).

The beds above these abnormal zones is diffusely stratified to massive, appears to be reworked in places, or disturbed, and exhibit sets of "backset lineations" with very steep angles that are organized in lenses ca.1 cm thick and 15 to 20 cm long (Fig 10D). The nature of these "lineations" is unclear, and could either be attributed to constructive laminae, to the underlining of regressive truncations, or they could represent a reworked facies.

"*Crocodile mouth"*:

A bedform of the "elongate type" (see Douillet et al. 2013b) exhibits a coarse-grained and massive layer that has a "crocodile-mouth" configuration on the upper stoss face of the bedform the layer (ca. 9 cm thick) locally splits into an upper layer (ca. 6 cm thick) and a 15 cm long basal part (ca. 3. cm thick), separated by a lamina set of fine-grained sediments in between (Fig 11). The sandwiched laminasets are deformed in a chevron-like pattern, whereas the basal layer shows a pickled basal surface that intrudes into the underlying contact. Directly downstream from the crocodile mouth, and emanating from the base of the split layer, a slip surface is encountered that displays a short throw in the downstream and upward direction with an angle of ca. 15º. Around 60 cm further downstream, a coarse-grained lens resembling the basal layer appears in the section and may be a prolongation of this basal bed.

"*Steep overturning truncations"*:

Very steep truncations are visible on the stoss sides of bedforms, and can reach dip angles above 80º. Some of these truncations are further underlined by a cm-thick zone where truncated laminae are coherently overturned over distances of up to tens of cms. These structures are referred to as "Steep Overturning Truncations, SOT". The formation of SOT was reproduced in lab experiments where short-lived air jets impacted on a stratified surface (Douillet et al. 2017). These structures are reported in the location maps of the shark-fin structures, since shark-fin patterns may develop in-train with the crests of SOT zones, but are the focus of a forthcoming manuscript.

3. Interpretation

The interpretation is based on the common shark-fin patterns observed in the deposits, and points toward stable waves that develop at a shear horizon as the physical explanation for the formation of shark-fins (this chapter). The inference of this process then enables to build a physical model in order to further constrain the stability of the structures (chapter 4). The anecdotic patterns are treated separately in the discussion, as the evidences point toward different triggers such as slumps, saltation impacts, or intraflow/collisions (chapter 5). Such processes may form structures resembling shark-fins but result from completely different dynamics.

3.1. General flow conditions

The fields of dune bedforms produced by the 2006 eruption of Tungurahua have been interpreted as deposited from diluted pyroclastic currents (Douillet et al. 2013a, 2013b). The mm-thickness of laminae most likely resulted from fluctuating and pulsating conditions in the current affecting sedimentation, and turbulence remains the best potential explanation for these laminations. This inferred occurrence of turbulence and the preserved laminations point toward a parent flow dominated by the dynamics of the fluid phase rather than by particle interactions. This further implies a rather low particle-concentration, falling in the field of "traction-dominated flow boundary zone" of Branney and Kokelaar (2002).

The shark-fin shapes are however unlikely to result from sedimentation from purely low concentration flows in fallout or saltation, since such processes usually produce laminae that are locally sub-planar on the faces of a bedform (even if only of ripple size). Given that many of the shark-fins are truncated, and covered by planar laminae, it is very likely that the process of overturning occurs briefly after deposition, and before or during sedimentation of the directly overlying beds. This points toward the occurrence of a syn-flow, superficial shearing. As already pointed by Allen and Banks (1972) for conventional overturned beds, the unidirectional alignment with the downflow/main-slope direction suggests a mechanism driven by the transport of the flow. Our interpretation is that the basal shearing of the flow is the cause.

In order to preserve the coherence of the lamination, the bed movement forming shark-fins must occur as packages rather than repose on the moving of particles individually. Accordingly, saltation, where particles are moved individually is not an adequate process (e.g. Douillet et al. 2014). On the contrary, the maintenance of the bed coherence requires a flow, which was sufficiently concentrated and which yielded sufficient strengths to deform the underlying bed. We therefore suggest that thin granular flows (possibly basal traction carpets, see Sohn 1997) triggered flow-bed interactions in the form of superficial granular shear.

Given that trains of shark-fins can include indifferently the convolute and two truncated types, we interpret that the three types result from a similar process. Furthermore, since truncated shark-fins follow the same dimensional trends as convolute ones, but with a lesser thickness, one may postulate that truncated ripple shark-fins are truncated versions of the convolute ones.

3.2. A stable wave interface at a shear horizon

The repetitive nature on the same horizon (in-train structures), together with the occurrence of a pseudo-wavelength (modulo harmonics) further suggest that the forming process behaves as a wave, i.e. an oscillatory mechanism with a wavelength, periodicity, and frequency. It follows that the numerous signs of disturbance directly upstream of shark-fins, or along a horizon containing shark-fins can be interpreted as the mark of shark-fins migrating laterally. These signs would thus represent the lateral displacement of the parent waves. At Villa Rica, Pajeras et al. (2010) already noted "subtle erosion and amalgamation surfaces", possibly related to the same processes. This strengthens the reasoning of Rowley (2010) on the seldom occurrence of shark-fins: "The structures [might] exist but migrate laterally through a steady current, leaving no recognizable feature other than a well mixed zone in their wake".

Similarly, shark-fins can be found in clusters that project on close-by lateral positions in successive laminae, so that a relative spatio-temporal stability during aggradation may also be inferred. Again, the observation strengthens the hypothesis of Rowley (2010) on the infrequent occurrence of shark-fins: "[Pyroclastic current] flow boundary zones [might] migrate vertically too rapidly for K-H-like [i.e. shark-fins] instability growth to occur". The jump of a shark-fin over several laminae thus suggests that the process(es) forming these waves has the same temporal scale as the aggradation rate, and that the bed configuration at a particular place is prone to trigger the formation of wavy shear interfaces. This latest suggestion is further supported by the fact that numbers of the waves are found in several isochrones directly behind a crest or a local break in slope of the paleo-topography. Noteworthy, Kuenen (1953) described folded beds associated with ripple beds (possibly due to pressure drops on the lee of the bedforms) whereas in the context of sheath folds, Cobblod and Quinquis (1980) noted that "passive folds can develop by kinematic amplification of deflections". All together, these information point toward the occurrence of stable waves at the flow-bed interface that formed in response to the bed configuration and other local conditions.

3.3. Pure shear vs. granular Kelvin-Helmholtz instabilities

Several studies have pointed out that wavy patterns can occur at the boundary between two granular mediums (Goldfarb 2002, Verhagen et al. 2013, Farin et al. 2014). Some authors have related shark-fin patterns to granular Kelvin-Helmholtz instabilities (Rowley et al. 2011, Farin et al. 2014, Douillet et al. 2015, Gladstone et al 2017) or showed through relationships of the Richardson number (ratio of buoyancy over shear forces) that density may have an influence (Verhagen et al. 2013). Kelvin-Helmholtz instabilities are related to a density interface that is subjected to shear and forms waves (i.e, the interface responds with a periodic oscillation), for which the restoring force is the density contrast at the interface. The wavy interface then evolves in vortices' shapes, which produce the typical patterns found in numerous analogue fluid experiments or atmospheric clouds.

In order to advance any interpretation in terms of Kelvin-Helmholtz instabilities, one would expect to find evidence for a potential influence of the restoring gravity force acting on a density interface in the deposits. In terms of sedimentological evidences, this might be expressed as the tail of the shark-fins being bent downwards (due to their excess weight compared to the overlying shearing fluid). None of the patterns observed in this study exhibit such a configuration, weakening the case for Kelvin-Helmholtz structures. Further, the experiments of Goldfarb (2002) produced vortical, repetitive in-train wave instabilities at a vertical interface, therefore not involving density but rather the competing shear and extensional strains as destabilizing and restoring forces. The grain size distribution of both affected and overlying beds are variable, and no rules concerning a possible bed density inversion was observed, in contrast to the suggestion in other deposits (Gladstone et al. 2017). We thus refrain here from interpreting density as the main restoring force for shark-fin structures, and thus, to interpret Kelvin-Helmholtz instability.

4. Theoretical framework

4.1. Model

A theoretical framework is developed below in order to translate the observation of the natural deposits (wavelength, thickness of deformation zone) to quantitative estimates of the parental flow values (Annex 2). Given that an oscillatory wave signal is present and that the form of the shark-fins points toward shearing, but that no insight enables to prove any influence of gravity as a restoring force, two theoretical frameworks were developed. We refrain however from using the Kelvin-Helmholtz equations for this analysis for the reasons outlined above.

The problem (Fig 12, fully developed in Annex 2) is considered with initial conditions consisting of two infinite and incompressible fluids with two different constant velocities in the horizontal direction. A shear horizon of thickness "$2*d$" separates the two fluids parallel to the flow direction. Within the shear horizon, a linear (laminar) velocity gradient is considered, representing the effect of viscosity (which is otherwise ignored in the standard Kelvin-Helmholtz instability problem, see e.g. Douillet et al. 2015). The initially horizontal upper and lower interfaces of the shear horizon are perturbed with a low amplitude wave ("η" with wavelength "λ"), and the analysis tackles the stability of these interfaces. The momentum and continuity equations are resolved for small perturbations.

The problem consists in quantifying the growth rate of the wave interface. The two frameworks differ only in their initial configurations: the first one considers a constant density for the problem, whereas the second considers a linear vertical density profile for the upper and lower mediums, but a constant density within the shear layer (considering the assumption of incompressibility, density can be advected but not diffused).

4.2. Results

The dispersion equations ruling the growth rate of the waves were resolved numerically (Fig 13). Three variables intervene in the equation: (i) the wavelength "λ" as observed in the natural deposits, (ii) the thickness of the shear horizon "$2*d$", which is approximated through the observed thickness of deformation, and (iii) the flow velocity "U". The output is a map of the growth rate of the waves, i.e. the rate of increase in the waves' amplitude (Fig 13).

4.2.1 Growth rate and sedimentation rate

The flow velocity is the only time-related quantity of the problem to which the growth rates of the waves' amplitude may be related, but these flow velocities are fairly loosely constrained in the results (Fig 13). Consequently, we approached the problem of discussing this growth rate through its comparison with plausible sedimentation rates (deposition rates) for pyroclastic currents. Indeed, if the sedimentation rate is much higher than the growth rate, then no structures would have time to form, but if the growth rate is much larger than the sedimentation rate, the structures are likely to have completely mixed the interface before they become frozen (buried). Further, since the natural shark-fins are climbing up the lamination (Fig 8), growth rates and sedimentation rates must be of comparable orders.

Growth rates reaching meters per seconds seem absurd and not likely to enable the preservation of shark-fins, at least for most progressive aggradation cases not invoking "*en masse*" processes. In their large scale pyroclastic current experiments, Breard et al. (2016) reported aggradation rates of 3.5 mm/s for crudely laminated layers but rates as fast as 450–550 mm/s for their main unit. Bracket values of 0.001 to 0.5 m/s are thus kept as the broad interval considered as realistic sedimentation rates and thus growth rate intervals. We further postulate that on one side, lamination likely develops in the lower range of these values. On the other side, we consider that large structures may be formed at higher sedimentation rates than smaller ones. Indeed, a thick shear horizon to create thick shark-fins may be either establishes through a larger thickness of the dense basal portion of a flow, or through a partitioning of the shear deeper in the deposit, both mechanisms likely occurring at high sedimentation rates only.

4.2.1. Result interpretation

The ratio of λ/d is a notable dimensionless quantity that determines the stability of the wave interface (Fig 13): For a constant density profile, a ratio of ca. 9 marks the limit between stable and unstable conditions, irrespectively of a flow velocity (Fig 13A). For very low velocities, very flattened patterns (i.e. high λ/d) seem to be stable as well, possibly representing slump events. Including a density gradient (Fig 13B), the stability can be expressed as a function of the Richardson number (i.e. the ratio of restoring density force and perturbing shear force), and as such does not explicitly expose a flow velocity. The observed patterns are comparable with other analyses of stability (e.g. Sutherland 2005).

Here, three cases are exemplified (d=3 cm, 10 cm, 1 m) both with constant density (Fig 14) and density gradient models (Fig 15). Since the posing of the problem solely involves λ and d as length quantities, and that the dependency on flow velocity (U_0) is very low, the patterns on the graphs are solely influenced by the λ/d ratio. Nevertheless, the examples are useful for visualization purposes. A deformation thickness of d= 3 cm is appropriate for the Tungurahua shark-fins varying from 0.3 to 5 cm thickness (Fig 14A, Fig 15A). Larger values are adequate for other case studies: e.g. d= 10 cm (Fig 14B, 15B) for turbidite convolute laminae (Gladstone et al. 2017), or d= 1 m (Fig 14C, 15C) for the large-scale shark-fin patterns observed at Mt. St. Helens (Brand et al 2017). Zones of small growth rates where shark-fins could potentially occur are highlighted in blue, while the zones we consider as optimal or limit growth rates are marked in green. Growth rates represented by warm colors are unlikely to preserve shark-fins because extremely high values likely destroy any sedimentological signature. The "constant density model" for a 3 cm shear horizon yields a strong cutoff for wavelengths around 30 cm (close to the natural observations), with growth rates abruptly increasing above this limit. Any wavelength below the cutoff is stable, which in turn explains the large span of thickness vs lengths within a narrow window of dimensions observed in nature (Fig 6). The "density gradient model" results in much more stable waves because of the restoring effects of density. The results of the theoretical framework thus suggest that the preservation of shark-fins is feasible for the whole range of tested values, and support the interpretation (Fig 15, 16).

5. Discussion and alternative interpretations

5.1. Questions surrounding the occurrence of shark-fins

Under the assumption that shark-fins are related to a combination of wave and shear mechanisms (Fig 16), three main questions arise The first one is to understand which bed conditions promote shark-fin formation. Liquefaction or fluidization is often emphasized for SSD formation (e.g. Roche et al. 2013, Verhagen et al. 2013, Baas et al. 2014, 2016). Yet whether liquid-like state is a necessary condition is unclear and we see no evidence for a liquid-like granular state around shark-fins. Note however that numerous small-scale impact sags are present, suggesting that the bed was in a relatively uncompacted, metastable state shortly after deposition. At more than 6 km distance from the crater, such impact sags are unlikely related to direct ballistic clasts, rather to anecdotic large particles landing from the pyroclastic currents.

A second question concerns the size that shark-fin structures can achieve under a wave-and-shear mechanism. The thickness of deformation shall be related to the cohesion strength of the bed, which shall be high enough to achieve a transfer down into the substrate. The strength necessary to produce a thick disturbance could be likely to destroy the upper part of the bed, so that shark-fins may be limited to a skin effect of a few centimeters. Most experimental work produced very small structures with a size comparable with our field examples (Rowley et al. 2011, Farin et al. 2014, Verhagen et al. 2013). Recently Pollock et al. (2017) were able to vary the size of vortices formed during pneumatic granular experiments, yet their setup as well was limited to structures no more than few centimeters in thickness. Other alternative explanations may be more relevant for meter scale features producing overturning (see 5.2.3.)

Finally, a broader question fosters on the possible occurrence of shark-fin patterns in other types of environments. In the case of a basal shear instability, the preservation of shark-fin is limited to environments with a high sedimentation rate, in order to preserve such structures in the deposits. Further, if a traction carpet has to occur to trigger sufficient shear stress, a high bedload transport is needed. Such conditions are likely achieved only for oversaturated decelerating flows, as already previously suggested (Douillet et al. 2013b, 2015). Given that a shear is present, a lateral current is involved, yet if saltation was dominating, the individual transport of clasts would result in the removal of the shark-fins. We thus suggest that shark-fins are produced under conditions of high sedimentation rates and below the threshold for saltation of deposited material, which has been referred to as "differential draping" conditions (Douillet et al. 2013b). Such conditions are most likely occurring in turbidity currents, glacial outburst flows or tsunamis, but not in rivers and aeolian environments, and indeed, most documented outcrops come from turbidites (Dzulynski Smith 1963,Larsen 1986, Butler et al. 2015, Gladstone et al. 2017), tsunamis (Matsumoto et al. 2008), or pyroclastic currents (Crowe and Fisher 1973, Pajeras et al. 2010, Rowley 2010, Douillet et al. 2015).

5.2. Alternative interpretations based on the anecdotic patterns

Our preferred interpretation to explain the formation of shark-fins is based on the occurrence of syn-depositional waves occurring at the shear horizon of the flow-bed boundary (Fig 16). However, several alternative interpretations can be discussed and the anecdotic patterns documented here are strong arguments for the occurrence of other mechanisms, in at least some cases (Fig 17). Future studies will hopefully be able to address these alternatives to provide an even more solid interpretation.

5.2.1. Slumping:

The lunate bedform outcrop (Fig 10) provides strong arguments for slumping as a mechanism of deformation (Fig 17A). Indeed, the anecdotic zones are situated on steep lee sides (>20º) prone to gravitational destabilization. Their lateral continuity over 2.5 m and consequent thickness (>15 cm) suggest a larger scale process as the waves envisaged before, and the unconformities forming the basal scars are hardly explained by an erosive event. Further, the disturbed zones are compound of a relatively massive mixture, as if the material were mixed by a mass movement. On top of that, the downstream ends of disturbed zones contain deformation structures linked with a shortening (Fig 10C, 9E), whereas the step-like "crinkled" forms at the onset seem to be related to extension (Fig 10B). This would suggest brief destabilizations of the steep lee side of the bedform, swaying under the combined action of the frontal (stoss) push of the pyroclastic currents, the rapid loading from the depositing mass, and oversteepening of the bedform (Fig 17A). It is unclear at which moment of the bedform formation such local slumps would occur, but the upper part of the bedform may have been affected, leading to the unexplained massive nature as well as the centimeter-scale sub-vertical lineations found on the upper part of the lee side.

Slumping, collapse or dynamic liquefaction has been involved in many previous interpretations for aeolian deposits -that share the property of having air as the interclast fluid with pyroclastic currents- (Allen and Banks 1972 and references therein, Chan et al. 2014, Ford et al. 2016). Although involving seismic liquefaction, Horowitz (1982) invokes “an unequally distributed surface load created by sand dune topography“ to explain the deformed layers in aeolian dune foresets. Thus, slumping could be an alternative interpretation to the wave instabilities, yet over very short distances, in order to at least partially preserve the deformed structures.

5.2.2. Impact sag trains

The recurrence of shark-fins has been interpreted as indicating a trigger occurring as a periodic wave, but other types of processes can produce such cyclic overturned beds without being waves. Further, there is no satisfactory restoring force if a wavy phenomenon is involved: a granular medium is unlikely to yield a sufficient surface tension, and the scale and geometry of the shark-fins makes it unlikely for buoyancy to be involved. The bouncing of a clast that would locally produce small impact sags and truncate beds could possibly explain the shark-fins (Fig 17B). Since a bouncing clast is expected to have a more or less recurrent jump length, this could well explain the regular distance between shark-fins. Numerous small-scale impact sags are present in the deposit, proving that the beds could be easily deformed. Further, examples documented from the Laacher See eruption revealed deformation structures from meter-scale impact sags producing patterns similar in many ways to the shark-fin geometry (e.g. Fig. 4 in Douillet et al. 2015). We have no argument to rule out bouncing clasts as a trigger for the formation of shark-fins for at least some of the structures documented here.

5.2.3. Collision and intraflows

The "crocodile mouth" found in the outcrop from the elongate bedform is singular (Fig 11). The configuration shows that the basal part of the flow locally penetrated at the base of the finer-grained sandwiched layer to form a small-scale injectite, whereas the top of the flow kept overriding the whole, but the causes are unclear (Fig 17C-D). Two mechanisms suggested in the literature could explain the resulting outcrop:

-The "bulldozer effect" evidenced and modeled for rock glaciers (Morgenthaler & Frehner 2017), where the slow and heavy mass of the flow folds and pushes the bed at the front. This would well explain the "chevron-like" deformed laminae in the sandwiched layer and the small thrust fault.

-The intraflow turbidity current experiments from Baas et al. (2014, 2016) may also explain the crocodile mouth, and share many features with our observations. In particular, these authors were able to experimentally produce a zone of mixing around the injectite, some nodules at the interface, and the sandwiching of the penetrated layer.

In our example, the accommodation of shortening in the sandwiched layer is testified through chevrons-like deformed laminae as well as the small thrust fault visible further downstream (Fig 17D). The sandwiched bed was thus squeezed. Without further evidence to distinguish between bulldozer- or intraflow-related shortening, we use the umbrella term "collision" to refer to a flow that pushed laterally the deposits underneath. A collision mechanism might be particularly relevant for larger scale features of overturning. For the case where one single overturned structure is present, collision may be a more suitable interpretation than a wavy shear interface to explain such structures.

Several questions cannot be answered here. It is unclear whether the sandwiched laminaset was part of a continuous layer that was otherwise eroded away, or was a local lens deposited in the "pool" formed by the stoss of the bedform. Although the disturbing bed is coarser-grained, it remains unproven that a density contrast with the fine-grained sandwiched material was present at time of (de)formation, nor can we speculate on the cohesive strength of the bed.

Conclusion

Shark-fin pattern has been defined here as an umbrella term for structures with a local overturned nature confined to a narrow lateral extent. Such structures have been variously reported in the literature on turbidites, sporadically from pyroclastic currents, and are ubiquitous in the deposits of the dilute pyroclastic currents from the 2006 eruption of Tungurahua. The rapid sedimentation of a highly polydisperse mixture of clasts likely promoted the entrapment of consequent amounts of fluids, and so facilitated metastable conditions. On the steep sided flanks of pyroclastic bedforms, beds are further influenced by a destabilizing effect of gravity. This was probably an ideal ground for the onset of syn- and post-depositional soft sediment deformation and re-arrangements.

The overturning of shark-fins suggests a syn-depositional shear mechanism. The spatial organization of shark-fins as repetitive in-trains patterns along a single laminae points toward a conventional wave mechanism as trigger. Further observations also suggest the lateral migration and concurrent growth of structure during sedimentation.

A physical model for the stability of waves at the interface of a shear horizon was developed with and without influence of density stratification. The stability analysis of the model shows that wavy patterns can develop, and that the wavelength of those structures is mainly depending on the thickness of the shear horizon. The results deliver convincing growth rates for the wavy patterns in regards to other documented sedimentation rates, flow velocities, and dimensions, and support this interpretation. No evidence exists to support the interpretation of these features as frozen Kelvin-Helmholtz instabilities.

In the screening for shark-fin structures, other anecdotic types of deformation patterns have been evidenced and interpreted as resulting from different processes. Apart from waves at a shear horizon, three other syn-flow mechanisms could be involved to produce soft sediment deformation with shark-fin patterns: collisional flows on the previously deposited bed, syn-flow slumping, or impact sags. The collision mechanism appears like a unique mechanism and not applicable to shark-fins where a rhythmicity is invoked. If slumping is a viable mechanism, then it resulted in a displacement of a few centimeters only, and no evidence of displacement are present in the majority of the observations.

We foresee a risk of over-interpretation of shark-fin structures as related to granular Kelvin-Helmholtz instabilities. Key observations would be needed for an explanation involving Kelvin-Helmholtz instabilities: (i) a stable spatial recurrence on a single horizon, (ii) signs of migration, and (iii) insights of the restoring influence of density. The later can be evidenced, for example, by tails that are recumbent in the downward (vertical) direction. Without these observations, it cannot be avoided that overturned structures result from the passive development of folds by kinematic amplification of deflections or a collision mechanism forming a single shortening fold. For the case of Tungurahua, the stratal organization, morphometrics parameters, and physical model all converge toward an explanation as syn-depositional waves at the interface of a shear horizon under very high sedimentation rates.

Figure captions

Figure 1: Sketch of the general morphology of shark-fin patterns and the measurements carried.

Figure 2: Sketch representing the three types of shark-fin patterns recognized in the outcrops.

Figure 3: Convolute shark-fin structures. A. Train of 2 convolute shark-fins, the first one truncated by a major truncation and with an angular shape, the second composite with two nearby tails (Plate TrT1aP3, see Table in Annex 1). B. train of 2 convolute "bulbous" shark-fins downstream a crest. A fine-grained massive "ploughed" zone emanates directly above the shark-fins (Plate TrT2P5). C. Fine-grained and massive shark-fin in a disturbed zone (Plate LuTNP2). D. Anecdotic coarse-grained angular shark-fin (Plate TrT4P6).

Figure 4: Truncated shark-fin structures. A-D Truncated ripple shark-fins: A. Plate TrT1aP4, B. Plate TrT1aP4, C. Plate TrP1aP3, D. Plate TrT3P6, E. Flat truncation shark-fins, Plate TrT1aP5.

Figure 5: Position of shark-fin patterns within the sediment plate outcrops by types. Structures in-trains are linked by black lines. For large scale image and details on the outcrops, see Douillet et al. in-sub-b. The code for each plate gives the bedform type and transect number.

Figure 6: Dimensions of shark-fin structures by types. Left side graphs are plotted versus length, right side versus thickness. The linear regressions are fitted by minimizing the euclidian distance between data and model after reducing and centering the data in order to account for the different length scales of the axes, and are calculated based on principal component analysis using the svd function in Matlab.

Figure 7: In train shark-fin organization. A. shark-fin separated with regular occurrence (Plate LuT2P3-P4). B. shark-fin separated by increasing distance (Plate TrT2P3). C. shark-fin downstream crest knick-point on the top right, Steep overturning truncation on stoss face, train of shark-fin within disturbed zone in the middle right, impact sag on lower left part (Plate LuTNP2a).

Figure 8: Clusters of migrating shark-fin (migration followed with pink dotted lines). A. Overturned laminae can be followed climbing stratigraphy with an initially downstream migration followed by two step-backs (Plate TrT4P2). B. A cluster of shark-fins is preceded upstream by zones of ploughed laminae (see Douillet et al. 2015). C. Cluster climbing lamination in the downstream direction with succession of truncated-convolute-truncated shark-fins (Plate LuTNP5).

Figure 9: Distance separating shark-fins in single trains. A) Non corrected data B. Data with inter-distance halved or divided by three to account for missed harmonics. When divided, harmonics are represented by black crosses between full-occurrences.

Figure 10: Anecdotic deformation zone. A. General view of Plate LuT2 with deformed zones highlighted in pink. Location of figures B-E are highlighted by white boxes. B. Onset of deformation with scars underlined by overturned laminae, unconformable contact, and step-like lamination on the upper right in the deformed beds. C. Zone of compression with overturned beds. D. The top part of the bedform contains lineations that form steep backsets, c.a. 1 cm thick and with pattern followed over tens of centimeters laterally. E. Zone of compression with cluster of convolute laminae coexistent in disturbed to massive zones.

Figure 11: Crocodile mouth structure. A. General view of Plate "Elongate" with location of deformation zone in Figure B marked with a white box. B. View of the crocodile mouth structure. C. Zoom into the onset of deformation, chevron-like structures, and pickled basal surface

Figure 12: Geometry of the physical framework.

Figure 13: Results of the stability analysis from the physical frameworks with the constant density model (A), and linear density gradient (B), with zoom, showing the growth rate of the perturbation as a function of flow velocity (A) or Richardson number (B) and the ratio of wavelength over thickness of shear layer.

Figure 14: Constant density model. Growth rate of the perturbation as a function of wavelength and flow velocity for different thicknesses of shear layer. Case A is most relevant to the Tungurahua shark-fins.

Figure 15: Gradient density model. Growth rate of the perturbation as a function of Richardson number and wavelength for different thicknesses of shear layer. Case A is most relevant to the Tungurahua shark-fins.

Figure 16: Interpretative sketch representing the process of formation of shark-fins. (A) In a regular setting, a fully turbulent boundary layer is developed down to the substrate. (B) If a basal granular flow is present in the form of a thin traction carpet, a shear horizon occurs, which reworks the superficial bed and creates shark-fins when the interface becomes wavy.

Figure 17: Interpretative sketches for the alternative explanations. A) the slumping mechanism for the lunate outcrop. B). In-train shark-fins might be related to the impact of saltating gravels. C) and D) The mechanism of collision forming the crocodile mouth via the flow of a dense granular flow over a fine-grained, metastable "pool".

Annex:

A1. Table of the shark-fin characteristics

Table caption A1:

Main characteristics of every encountered shark-fin structures.

<u>plate code</u>:

Lu (Lunate) or Tr (Transverse); T (Trench number); P (Plate number increasing from 1 to 6 in the downflow direction).

<u>Affected zone & overlying beds</u>:

-<u>face- slope</u>: S (Stoss), L (lee), F (Flat zone) C (Crest area). Slope is given in degree to the horizontal and positive when dipping against flow direction.

-<u>Grain size (GS) attribute:</u> (fin, mid, coa): fin: ~125 µm mid: 250 µm coa: 500 µm

-<u>Stratification (strat) attribute:</u> (CL / L / DL / M): crude and clear pronounced lamination (CL), normal well laminated (L), diffuse lamination only distinguishable with the impregnation method (DL) and massive (M).

-<u>Additional lamination attribute:</u> (DIST / W / BCKS / VERT / CHAOS): disturbed by deformation (DIST), Wavy laminasets (W), backset laminae (BCKS), vertical backset bedding (VERT), chaotic zone with hardly interpretable reason (CHAOS)

-<u>Additional lamina</u>(DIST / W / BCKS / VERT / CHAOS): disturbed by deformation (DIST), Wavy laminasets (W), backset laminae (BCKS), vertical backset bedding (VERT), chaotic zone with hardly interpretable reason (CHAOS)

<u>Overturned structure</u>:

L (Length of affected zone), T (Thickness of affected zone), N lam (Number of affected laminae), E (Elongation) D-next (Distance to next shark-fin, if in-train)

<u>Upper contact:</u>

Slope angle and Type: erosive (ER) or concordant (C)

<u>Lateral continuity & Comments:</u>

Same abbreviations as for the rest of table

<u>Position:</u>

Measured from upstream end of plate, vertical (vert) and horizontal (hor) position, as well as position within the 2006 sequence (seq): base (B), middle (M) or top (T).

A2. Physical framework

(separated document ANNEX2_Equations.docx)

Acknowledgements

GAD acknowledges funding of this project by the Deutsche Forschungsgemeinschaft grant DO1953/1-1. Several tests were done during a campaign funded by the "BayLat" agency to GAD (Bavaria-Latin-America exchange program). QC was funded by the Alsacian grant "Boussole" for his internship. M. Bouysson, I Holscher, R. Reschetizka and P. Witting worked as student assistants to mount the sediment plate exhibition through the "LMU-StudiForscht" funding scheme. DBD wishes to acknowledge the support of an ERC Advanced Grant (247076).

References

Allen, J. R. L., & Banks, N. L. (1972). An interpretation and analysis of recumbent-folded deformed cross-bedding. Sedimentology, 19(3-4), 257-283.

Allen J.R.L. (1982). Sedimentary structures, their character and physical basis (Vol. 2). Developments in Sedimentology 30B. Elsevier.

Baas, J. H., Manica, R., Puhl, E., Verhagen, I., & Borges, A. L. D. O. (2014). Processes and products of turbidity currents entering soft muddy substrates. Geology, 42(5), 371-374.

Baas, J. H., Manica, R., Puhl, E., & Oliveira Borges, A. L. (2016). Thresholds of intrabed flow and other interactions of turbidity currents with soft muddy substrates. Sedimentology, 63(7), 2002-2036.

Benage, M. C., Dufek, J., Degruyter, W., Geist, D., Harpp, K., & Rader, E. (2014). Tying textures of breadcrust bombs to their transport regime and cooling history. Journal of Volcanology and Geothermal Research, 274, 92-107.

Benage, M. C., Dufek, J., & Mothes, P. A. (2016). Quantifying entrainment in pyroclastic density currents from the Tungurahua eruption, Ecuador: Integrating field proxies with numerical simulations. Geophysical Research Letters, 43(13), 6932-6941.

Bernard, J., Kelfoun, K., Le Pennec, J. L., & Vargas, S. V. (2014). Pyroclastic flow erosion and bulking processes: comparing field-based vs. modeling results at Tungurahua volcano, Ecuador. Bulletin of volcanology, 76(9), 858.

Brand, B. D., Pollock, N., Sarocchi, D., Dufek, J., & Clynne, M. A. (2017). Field-trip guide for exploring pyroclastic density current deposits from the May 18, 1980, eruption of Mount St. Helens, Washington (No. 2017-5022-C). US Geological Survey.

Branney, M. J., & Kokelaar, B. P. (2002). Pyroclastic density currents and the sedimentation of ignimbrites. Geological Society of London.

Breard, E. C., Lube, G., Jones, J. R., Dufek, J., Cronin, S. J., Valentine, G. A., & Moebis, A. (2016). Coupling of turbulent and non-turbulent flow regimes within pyroclastic density currents. Nature Geoscience, 9(10), 767-771.

Breard, E. C., & Lube, G. (2017). Inside pyroclastic density currents–uncovering the enigmatic flow structure and transport behaviour in large-scale experiments. Earth and Planetary Science Letters, 458, 22-36.

Burgisser, A., & Bergantz, G. W. (2002). Reconciling pyroclastic flow and surge: the multiphase physics of pyroclastic density currents. Earth and Planetary Science Letters, 202(2), 405-418.

Butler, R. W., & Tavarnelli, E. (2006). The structure and kinematics of substrate entrainment into high-concentration sandy turbidites: a field example from the Gorgoglione 'flysch'of southern Italy. Sedimentology, 53(3), 655-670.

Butler, R. W., Eggenhuisen, J. T., Haughton, P., & McCaffrey, W. D. (2016). Interpreting syndepositional sediment remobilization and deformation beneath submarine gravity flows; a kinematic boundary layer approach. Journal of the Geological Society, 173(1), 46-58.

Chan, M. A. and Bruhn, R. L.: Dynamic liquefaction of Jurassic sand dunes: processes, Origins, and implications, Earth Surf. Proc. Land., 39, 1478–1491, 2014.

Cobbold, P. R., & Quinquis, H. (1980). Development of sheath folds in shear regimes. Journal of structural geology, 2(1-2), 119-126.

Cole, P. D. (1991). Migration direction of sand-wave structures in pyroclastic-surge deposits: implications for depositional processes. Geology, 19(11), 1108-1111.

Cole, P. D., Guest, J. E., & Duncan, A. M. (1993). The emplacement of intermediate volume ignimbrites: a case study from Roccamonfina Volcano, Southern Italy. Bulletin of Volcanology, 55(7), 467-480.

Crowe, B. M., & Fisher, R. V. (1973). Sedimentary structures in base-surge deposits with special reference to cross-bedding, Ubehebe Craters, Death Valley, California. Geological Society of America Bulletin, 84(2), 663-682.

Dellino, P., Isaia, R., & Veneruso, M. (2004). Turbulent boundary layer shear flows as an approximation of base surges at Campi Flegrei (Southern Italy). Journal of Volcanology and Geothermal Research, 133(1), 211-228.

Douillet, G. A., Tsang-Hin-Sun, È., Kueppers, U., Letort, J., Pacheco, D. A., Goldstein, F., ... & Robin, C. (2013a). Sedimentology and geomorphology of the deposits from the August 2006 pyroclastic density currents at Tungurahua volcano, Ecuador. Bulletin of volcanology, 75(11), 765.

Douillet, G. A., Pacheco, D. A., Kueppers, U., Letort, J., Tsang-Hin-Sun, È., Bustillos, J., ... & Dingwell, D. B. (2013b). Dune bedforms produced by dilute pyroclastic density currents from the August 2006 eruption of Tungurahua volcano, Ecuador. Bulletin of volcanology, 75(11), 762.

Douillet, G. A., Rasmussen, K. R., Kueppers, U., Castro, D. L., Merrison, J. P., Iversen, J. J., & Dingwell, D. B. (2014). Saltation threshold for pyroclasts at various bedslopes: Wind tunnel measurements. Journal of Volcanology and Geothermal Research, 278, 14-24.

Douillet, G. A., Taisne, B., Müller, S. K., Kueppers, U., & Dingwell, D. B. (2015). Syn-eruptive, soft-sediment deformation of deposits from dilute pyroclastic density current: triggers from granular shear, dynamic pore pressure, ballistic impacts and shock waves. Solid Earth, 6(2), 553.

Douillet G. A. (2017). Overturned strata in deposits of dilute pyroclastic density currents, field and analogue data. Abstract 1228. IAVCEI Scientific Assembly, Portland Oregon, 14-18.08.2017.

Douillet G.A., Kueppers U., Mato C. Bouysson M., Chaffaut Q., Reschetizka R., Dingwell D.B., Bernard B. (submitted-a) Revisiting the lacquer peels method with pyroclastic deposits: Sediment plates, a precise, fine-scale imaging method and powerful outreach tool. Journal of applied volcanology

Douillet G.A., Bernard B., Bouysson M., Broschat N., Chaffaut Q., Dingwell D.B., Holscher I., Kueppers U., Mato C., Schlunegger F., Witting P. (in submission-b). The three architectural elements for the formation of pyroclastic dune bedforms. Microscale sedimentary dynamics and lateral variations exemplified from the 2006 pyroclastic currents at Tungurahua (Ecuador). Sedimentology (this issue?)

Dufek J, Bergantz GW. 2007. Suspended load and bed-load transport of particle-laden gravity currents: the role of particle–bed interaction. Theor. Comput. Fluid Dyn. 21:119–4

Dufek, J. (2016). The fluid mechanics of pyroclastic density currents. Annual Review of Fluid Mechanics, 48, 459-485.

Ongaro, T. E., Neri, A., Menconi, G., Vitturi, M. D. M., Marianelli, P., Cavazzoni, C., ... & Baxter, P. J. (2008). Transient 3D numerical simulations of column collapse and pyroclastic density current scenarios at Vesuvius. Journal of Volcanology and Geothermal Research, 178(3), 378-396.

Ongaro, T. E., Widiwijayanti, C., Clarke, A. B., Voight, B., & Neri, A. (2011). Multiphase-flow numerical modeling of the 18 May 1980 lateral blast at Mount St. Helens, USA. Geology, 39(6), 535-538.

Eggenhuisen, J. T., McCaffrey, W. D., Haughton, P. D., & Butler, R. W. (2011). Shallow erosion beneath turbidity currents and its impact on the architectural development of turbidite sheet systems. Sedimentology, 58(4), 936-959.

Farin, M., Mangeney, A., & Roche, O. (2014). Fundamental changes of granular flow dynamics, deposition, and erosion processes at high slope angles: insights from laboratory experiments. Journal of Geophysical Research: Earth Surface, 119(3), 504-532.

Fisher, R. V. (1979). Models for pyroclastic surges and pyroclastic flows. Journal of Volcanology and Geothermal Research, 6(3-4), 305-318.

Gladstone, C., McClelland, H. M. O., Woodcock, N. H., Pritchard, D., & Hunt, J. (2017). On the formation of convolute lamination in mud-rich turbidites. Sedimentology, 1-43.

Goldfarb, D. J., Glasser, B. J., & Shinbrot, T. (2002). Shear instabilities in granular flows. Nature, 415(6869), 302-305.

Horowitz, D. H. (1982). Geometry and origin of large-scale deformation structures in some ancient wind-blown sand deposits. Sedimentology, 29(2), 155-180.

Houssais, M., Ortiz, C. P., Durian, D. J., & Jerolmack, D. J. (2015). Onset of sediment transport is a continuous transition driven by fluid shear and granular creep. Nature communications, 6.

Kelfoun, K., Samaniego, P., Palacios, P., & Barba, D. (2009). Testing the suitability of frictional behaviour for pyroclastic flow simulation by comparison with a well-constrained eruption at Tungurahua volcano (Ecuador). Bulletin of volcanology, 71(9), 1057.

Larsen, P. H. (1986). Soft sediment deformation structures in Silurian turbidites from North Greenland. Bull. Geol. Soc. Denmark, 35, 19-23.

Logan, W.E., 1863. Report on the Geology of Canada. John Lovell, Montreal, Canada, p. 464.

Lowe, D. R. (1976). Subaqueous liquefied and fluidized sediment flows and their deposits. Sedimentology, 23(3), 285-308.

Lube, G., Cronin, S. J., Platz, T., Freundt, A., Procter, J. N., Henderson, C., & Sheridan, M. F. (2007). Flow and deposition of pyroclastic granular flows: A type example from the 1975 Ngauruhoe eruption, New Zealand. Journal of Volcanology and Geothermal Research, 161(3), 165-186.

Maltman, A. (Ed.). (1994). The geological deformation of sediments. Springer Science & Business Media, Springer, Dordrecht

Marques (2012) Comment on "Eye and sheath folds in turbidite convolute lamination: Aberystwyth Grits Group, Wales", by H.L.O. McClelland, N.H. Woodcock, C. Gladstone, Journal of Structural Geology 33 (2011) 1140–1147. Journal of Structural Geology, 37, 248-250

McClelland, H. L. O., Woodcock, N. H., & Gladstone, C. (2011). Eye and sheath folds in turbidite convolute lamination: Aberystwyth Grits Group, Wales. Journal of Structural Geology, 33(7), 1140-1147.

McKee, E. D., Reynolds, M. A., & Baker Jr, C. H. (1962a). 164. Laboratory studies on deformation in unconsolidated sediment. US Geological Survey Professional Paper, 151.

McKee, E. D., Reynolds, M. A., & Baker Jr, C. H. (1962b). 165. Experiments on intraformational recumbent folds in cross bedded sand. US Geological Survey Professional Paper, 155.

Morgenthaler J., Frehner M. (2017). Bulldozer-like soil erosion at the front of a rockglacier indicates change in advance dynamics: Case study from the Furggentälti, Vallais, Switzerland. Swiss Geoscience Meeting, Davos 18.11.2017

Nichol, K., Zanin, A., Bastien, R., Wandersman, E. & van Hecke, M. Flow-induced agitations create a granular fluid. Phys. Rev. Lett. 104, 078302 (2010).

Owen, G., Moretti, M., & Alfaro, P. (2011). Recognising triggers for soft-sediment deformation: current understanding and future directions. Sedimentary Geology, 235(3), 133-140.

Palladino, D. M. (2017). Simply pyroclastic currents. Bulletin of Volcanology, 79(7), 53.

Parejas, C. S., Druitt, T. H., Robin, C., Moreno, H., & Naranjo, J. A. (2010). The Holocene Pucón eruption of Volcán Villarrica, Chile: deposit architecture and eruption chronology. Bulletin of volcanology, 72(6), 677-692.

Pollock N., Brand B., Roche O., Rowley P., Sarocchi D., Sulpizio R. (2017). Using shear-induced, wave-like depositional features to infer flow conditions of pyroclastic density currents at Mount St Helens, Washington, USA. Abstract 1081. IAVCEI Scientific Assembly, Portland Oregon, 14-18.08.2017.

Postma, G., Cartigny, M., & Kleverlaan, K. (2009). Structureless, coarse-tail graded Bouma Ta formed by internal hydraulic jump of the turbidity current?. Sedimentary Geology, 219(1), 1-6.

Postma, G., Kleverlaan, K., & Cartigny, M. J. (2014). Recognition of cyclic steps in sandy and gravelly turbidite sequences, and consequences for the Bouma facies model. Sedimentology, 61(7), 2268-2290.

Rader, E., Geist, D., Geissman, J., Dufek, J., & Harpp, K. (2015). Hot clasts and cold blasts: thermal heterogeneity in boiling-over pyroclastic density currents. Geological Society, London, Special Publications, 396(1), 67-86.

Rowley, P. J., Kokelaar, P., Menzies, M., & Waltham, D. (2011). Shear-derived mixing in dense granular flows. Journal of Sedimentary Research, 81(12), 874-884.

Rowley, P. (2010). Analogue modelling of pyroclastic density current deposition (Doctoral dissertation, Royal Holloway, University of London).

Roche, O., Niño, Y., Mangeney, A., Brand, B., Pollock, N., & Valentine, G. A. (2013). Dynamic pore-pressure variations induce substrate erosion by pyroclastic flows. Geology, 41(10), 1107-1110.

Shanmugam, G. (2017). Global case studies of soft-sediment deformation structures (SSDS): Definitions, classifications, advances, origins, and problems. Journal of Palaeogeography, 6(4), 251-320.

Sohn, Y. K. (1997). On traction-carpet sedimentation. Journal of Sedimentary Research, 67(3).

Sparks, R. S. J. (1976). Grain size variations in ignimbrites and implications for the transport of pyroclastic flows. Sedimentology, 23(2), 147-188.

Sulpizio, R., Dellino, P., Doronzo, D. M., & Sarocchi, D. (2014). Pyroclastic density currents: state of the art and perspectives. Journal of Volcanology and Geothermal Research, 283, 36-65.

Sulpizio R., Sarocchi D., Rodriguez-Sedano L. A., Brand B., Pollock N., Campos G. (2017). On the entrapment mechanisms of volcanic granular flows from laboratory experiments and comparison with natural exposures. Abstract 827. IAVCEI Scientific Assembly, Portland Oregon, 14-18.08.2017.

Verhagen, I. T. E., Baas, J. H., Jacinto, R. S., McCaffrey, W. D., & Davies, A. G. (2013). A first classification scheme of flow-bed interaction for clay-laden density currents and soft substrates. Ocean Dynamics, 63(4), 385-397.

Sutherland, B. R. (2005). Stratified shear flow: instability and wave radiation. WIT Transactions on State-of-the-art in Science and Engineering, 6.

Walker, G. P. (1984). Characteristics of dune-bedded pyroclastic surge bedsets. Journal of Volcanology and Geothermal Research, 20(3-4), 281-296.

Wohletz, K. H., & Sheridan, M. F. (1979). A model of pyroclastic surge. Geological Society of America Special Papers, 180, 177-194.

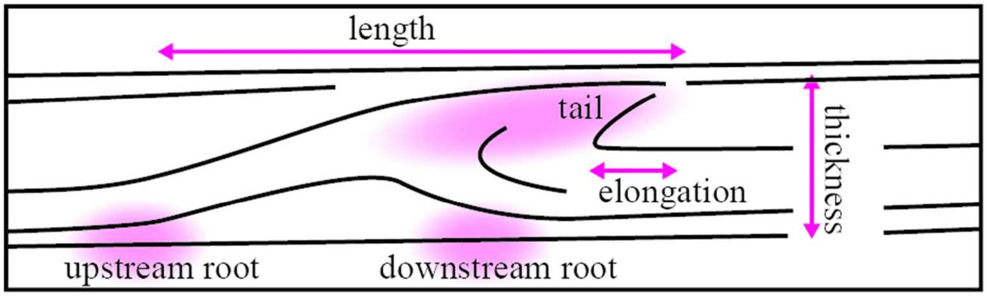

Figure 1: Sketch of the general morphology of shark-fin patterns and the measurements carried.

80x24mm (300 x 300 DPI)

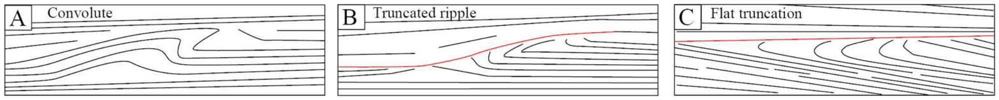

Figure 2: Sketch representing the three types of shark-fin patterns recognized in the outcrops.

180x18mm (300 x 300 DPI)

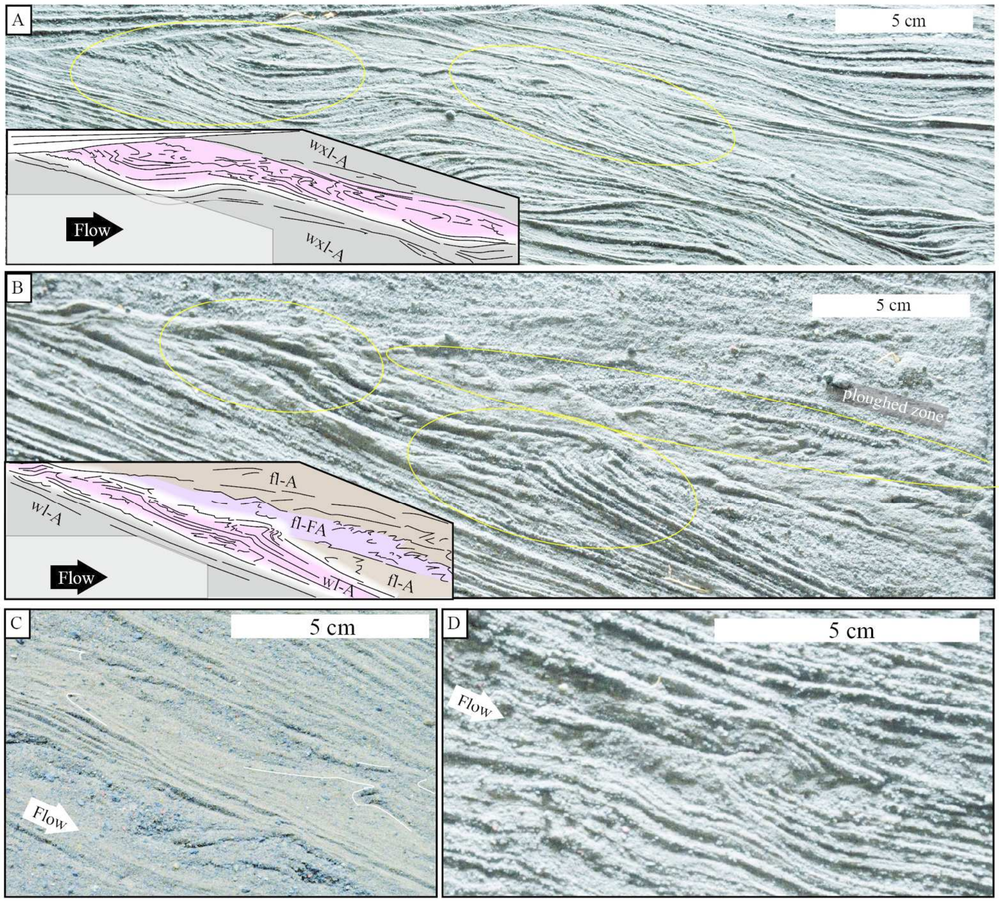

Figure 3: Convolute shark-fin structures. A. Train of 2 convolute shark-fins, the first one truncated by a major truncation and with an angular shape, the second composite with two nearby tails (Plate TrT1aP3, see Table in Annex 1). B. train of 2 convolute "bulbous" shark-fins downstream a crest. A fine-grained massive "ploughed" zone emanates directly above the shark-fins (Plate TrT2P5). C. Fine-grained and massive shark-fin in a disturbed zone (Plate LuTNP2). D. Anecdotic coarse-grained angular shark-fin (Plate TrT4P6).

180x162mm (300 x 300 DPI)

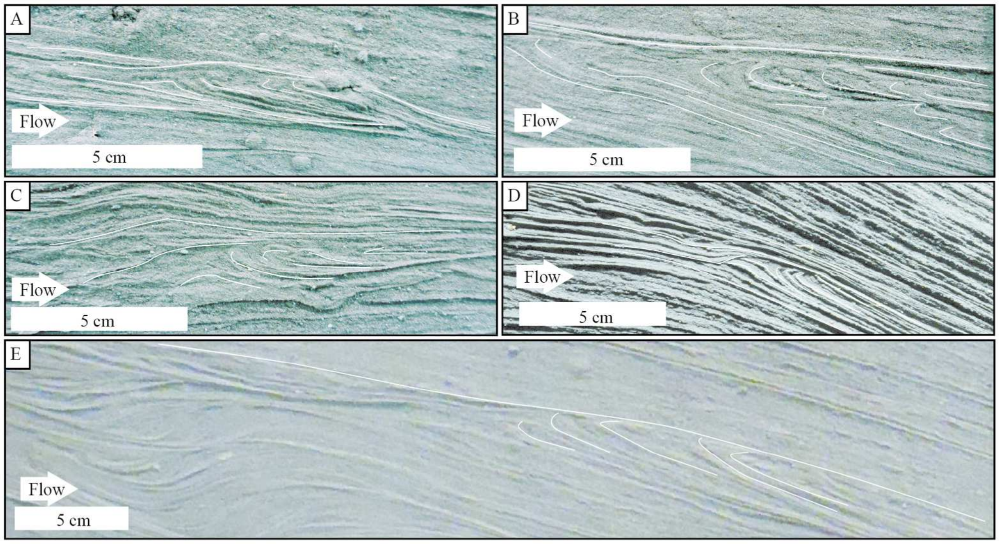

Figure 4: Truncated shark-fin structures. A-D Truncated ripple shark-fins: A. Plate TrT1aP4, B. Plate TrT1aP4, C. Plate TrP1aP3, D. Plate TrT3P6, E. Flat truncation shark-fins, Plate TrT1aP5.

180x97mm (300 x 300 DPI)

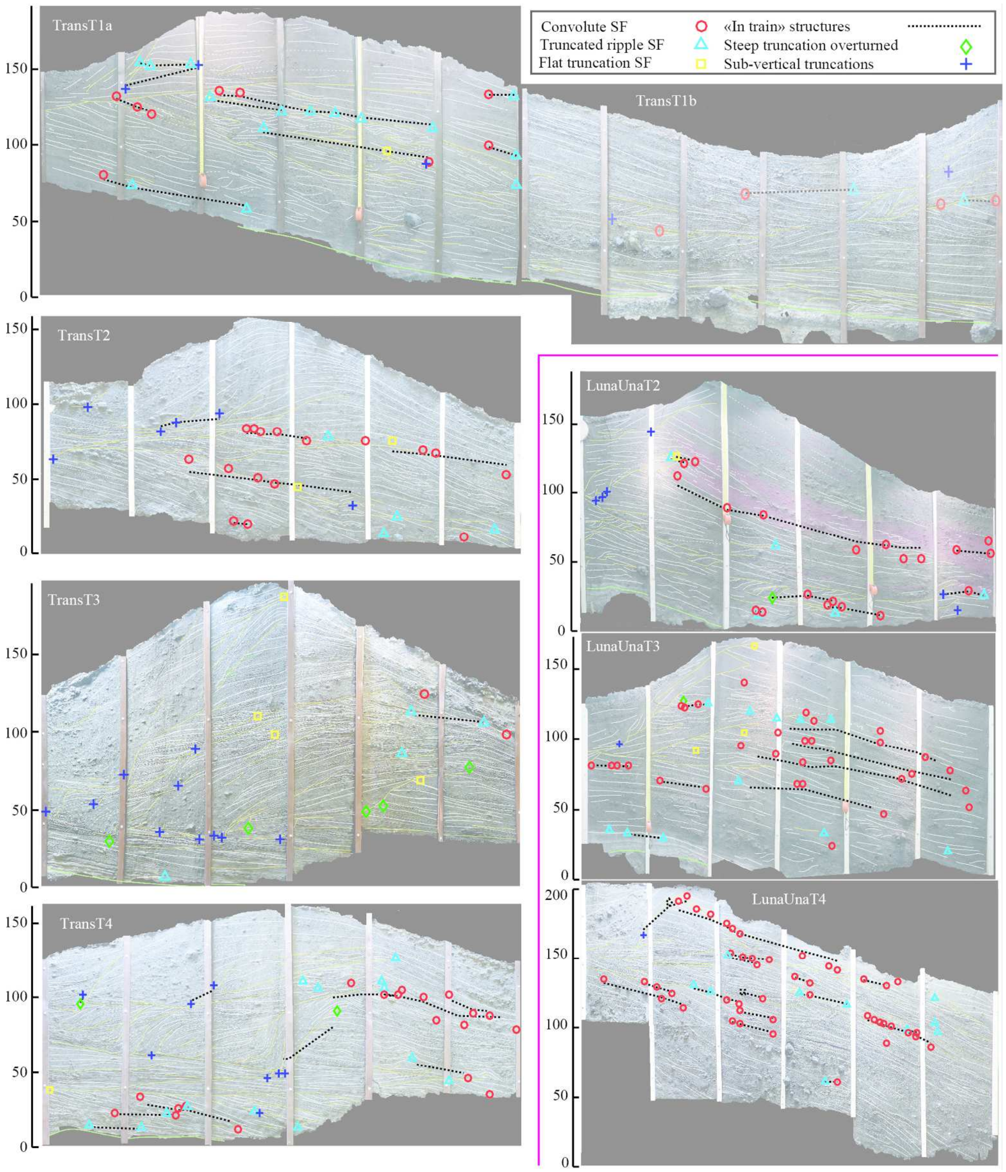

Figure 5: Position of shark-fin patterns within the sediment plate outcrops by types. Structures in-trains are linked by black lines. For large scale image and details on the outcrops, see Douillet et al. in-sub-b. The code for each plate gives the bedform type and transect number.

180x209mm (300 x 300 DPI)

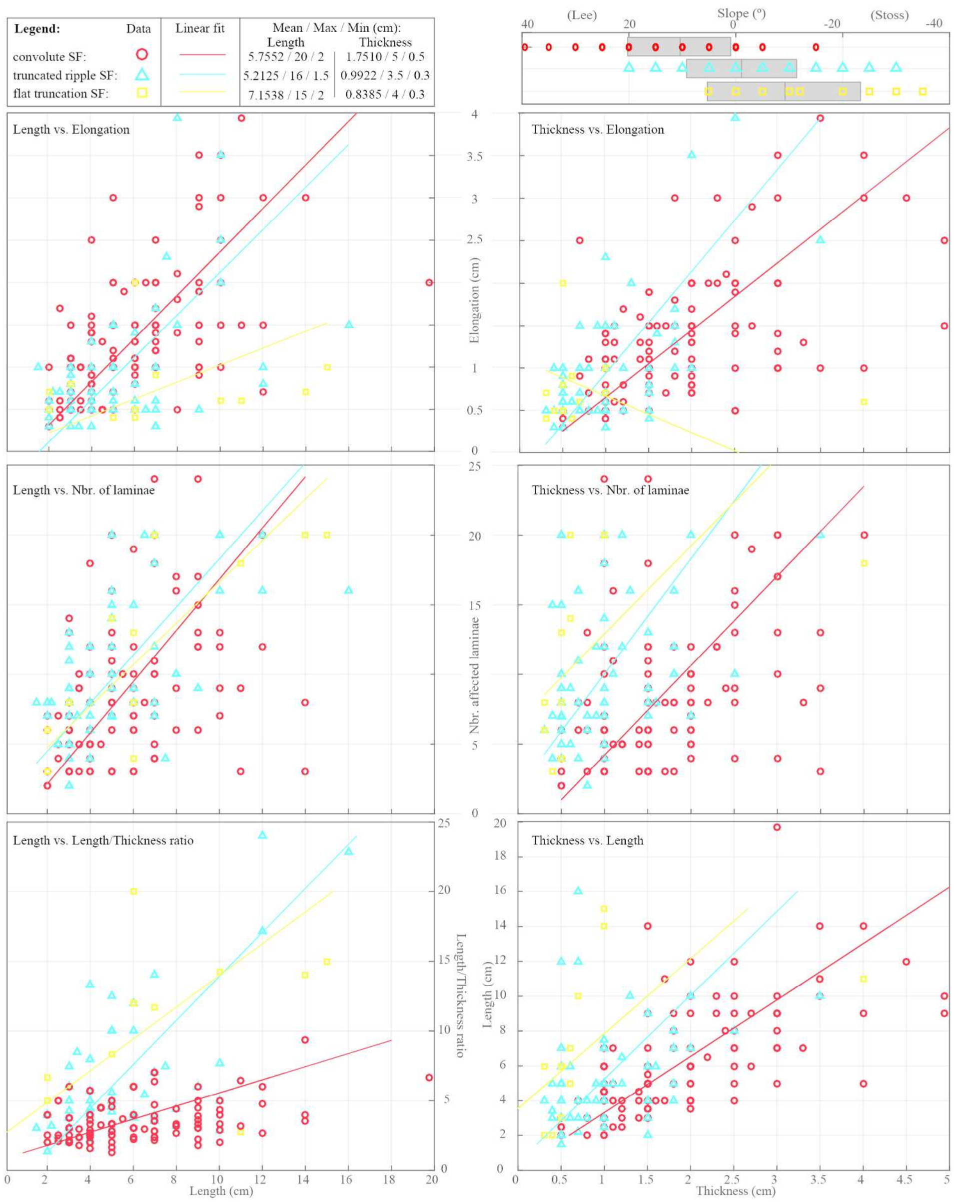

Figure 6: Dimensions of shark-fin structures by types. Left side graphs are plotted versus length, right side versus thickness. The linear regressions are fitted by minimizing the euclidian distance between data and model after reducing and centering the data in order to account for the different length scales of the axes, and are calculated based on principal component analysis using the svd function in Matlab.

180x224mm (300 x 300 DPI)

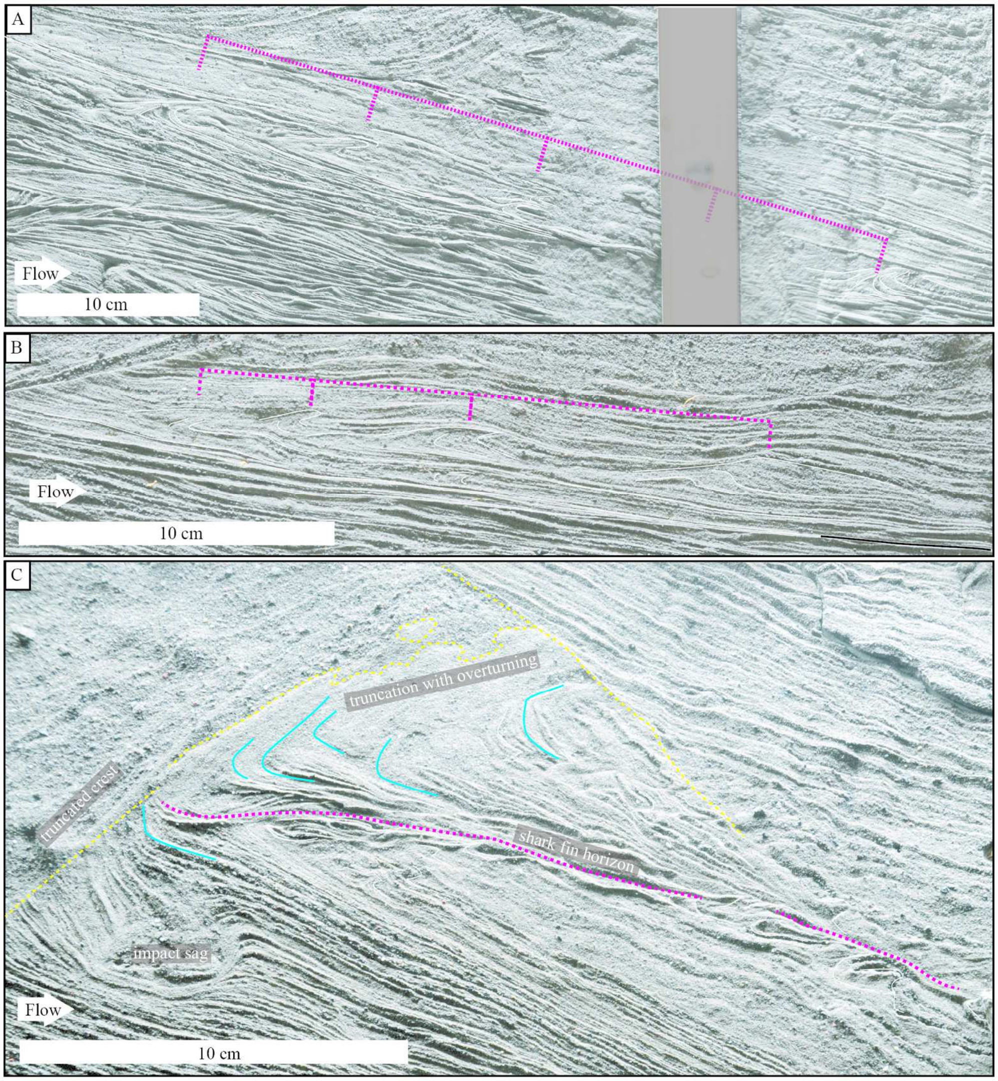

Figure 7: In train shark-fin organization. A. shark-fin separated with regular occurrence (Plate LuT2P3-P4). B. shark-fin separated by increasing distance (Plate TrT2P3). C. shark-fin downstream crest knick-point on the top right, Steep overturning truncation on stoss face, train of shark-fin within disturbed zone in the middle right, impact sag on lower left part (Plate LuTNP2a).

180x194mm (300 x 300 DPI)

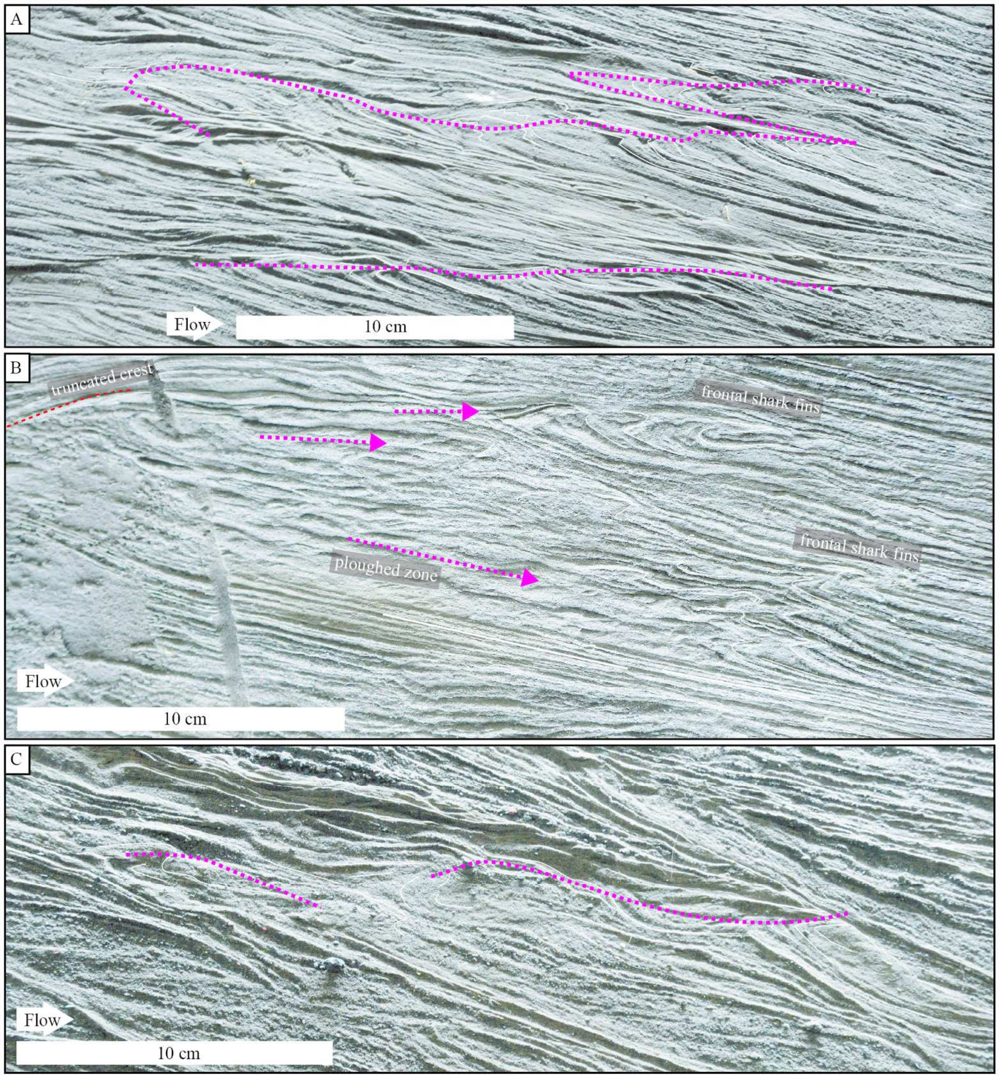

Figure 8: Clusters of migrating shark-fin (migration followed with pink dotted lines). A. Overturned laminae can be followed climbing stratigraphy with an initially downstream migration followed by two step-backs (Plate TrT4P2). B. A cluster of shark-fins is preceded upstream by zones of ploughed laminae (see Douillet et al. 2015). C. Cluster climbing lamination in the downstream direction with succession of truncated-convolute-truncated shark-fins (Plate LuTNP5).

180x193mm (300 x 300 DPI)

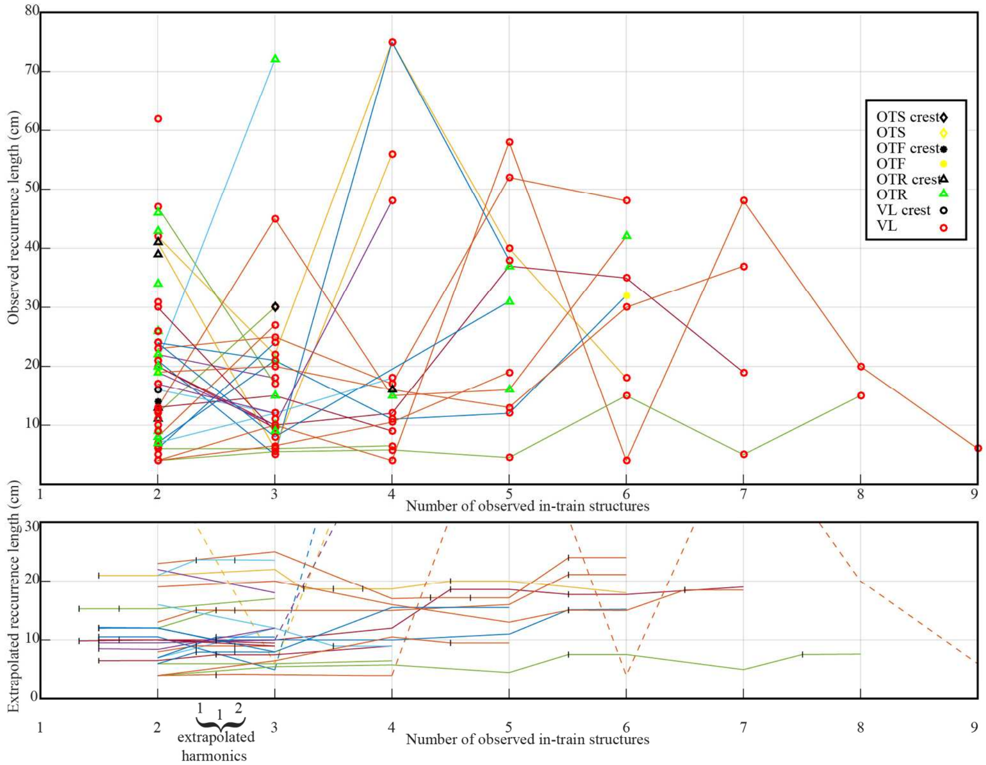

Figure 9: Distance separating shark-fins in single trains. A) Non corrected data B. Data with inter-distance halved or divided by three to account for missed harmonics. When divided, harmonics are represented by black crosses between full-occurrences.

180x140mm (300 x 300 DPI)

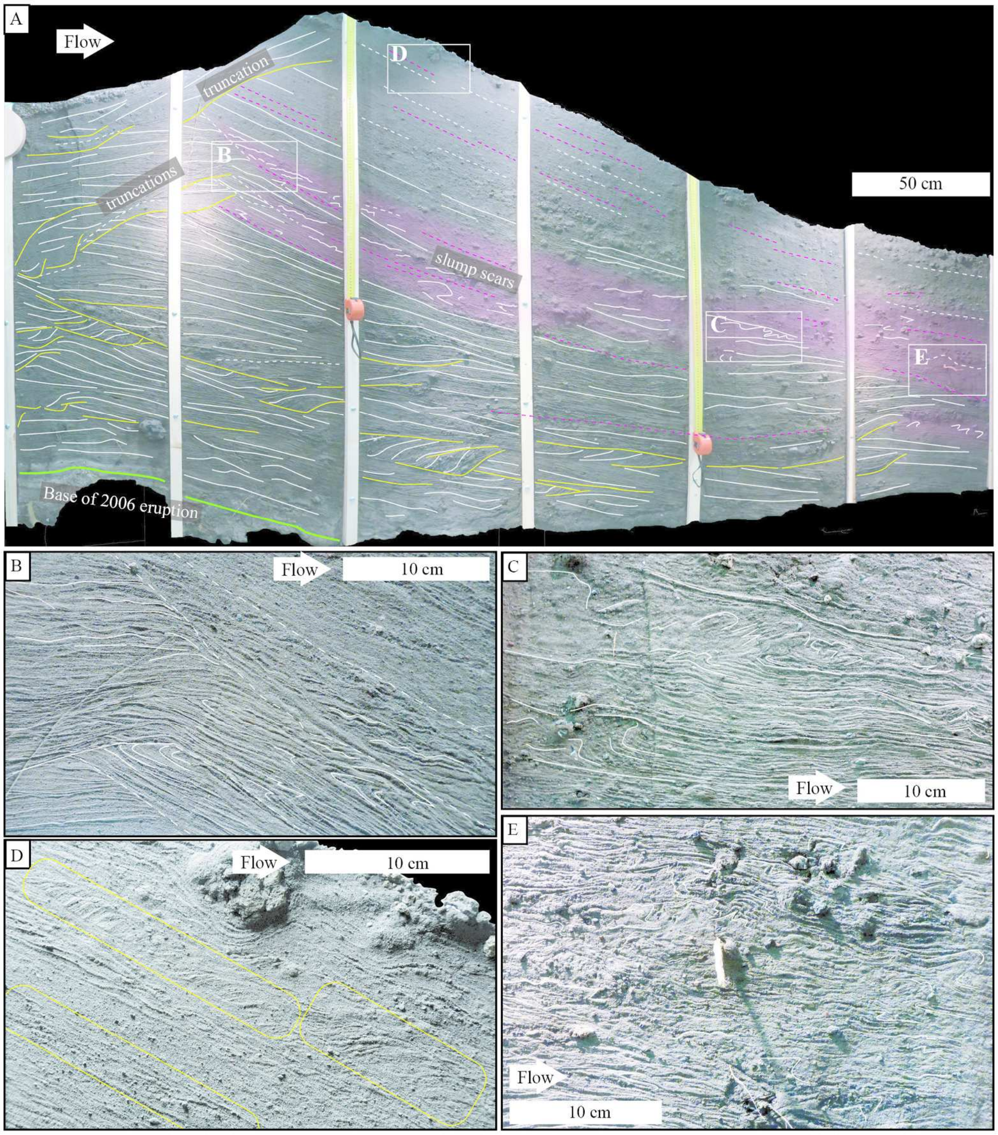

Figure 10: Anecdotic deformation zone. A. General view of Plate LuT2 with deformed zones highlighted in pink. Location of figures B-E are highlighted by white boxes. B. Onset of deformation with scars underlined by overturned laminae, unconformable contact, and step-like lamination on the upper right in the deformed beds. C. Zone of compression with overturned beds. D. The top part of the bedform contains lineations that form steep backsets, c.a. 1 cm thick and with pattern followed over tens of centimeters laterally. E. Zone of compression with cluster of convolute laminae coexistent in disturbed to massive zones.

180x204mm (300 x 300 DPI)

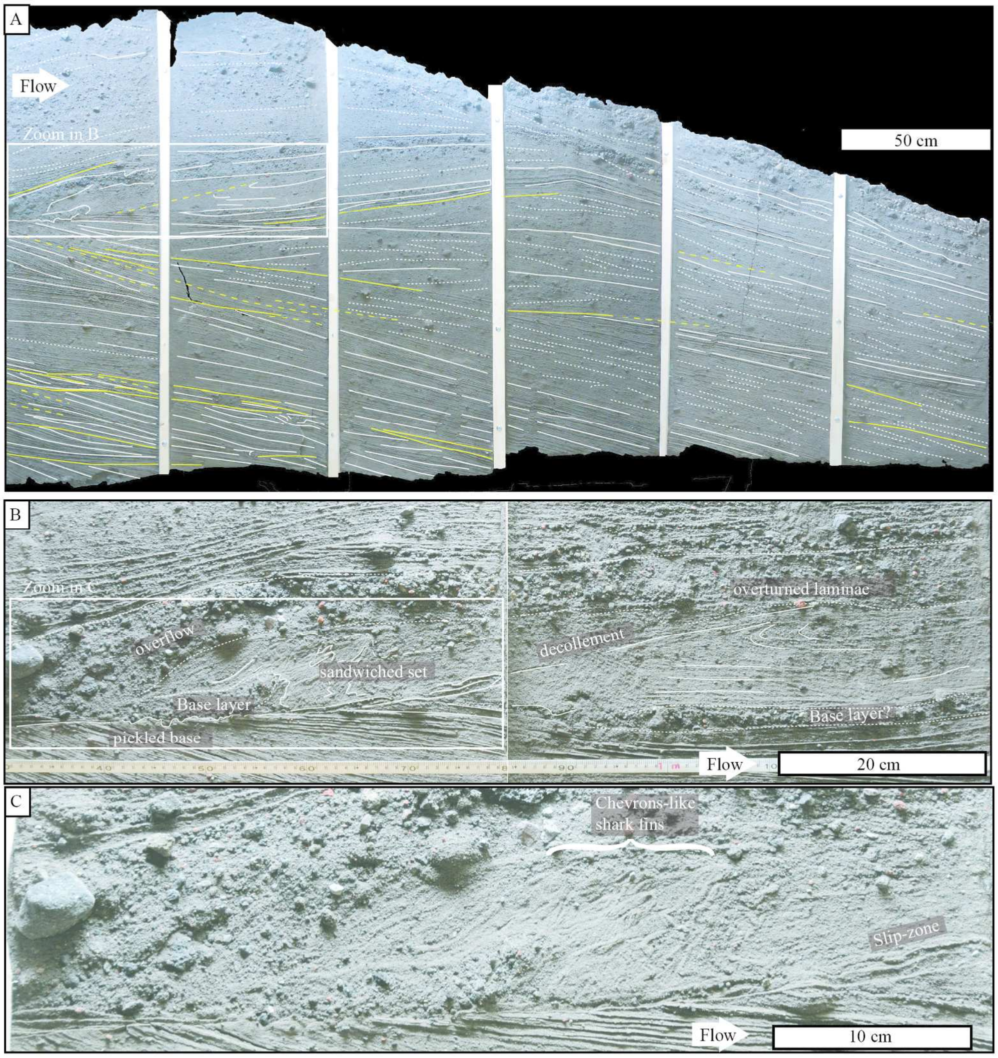

Figure 11: Crocodile mouth structure. A. General view of Plate "Elongate" with location of deformation zone in Figure B marked with a white box. B. View of the crocodile mouth structure. C. Zoom into the onset of deformation, chevron-like structures, and pickled basal surface.

180x189mm (300 x 300 DPI)

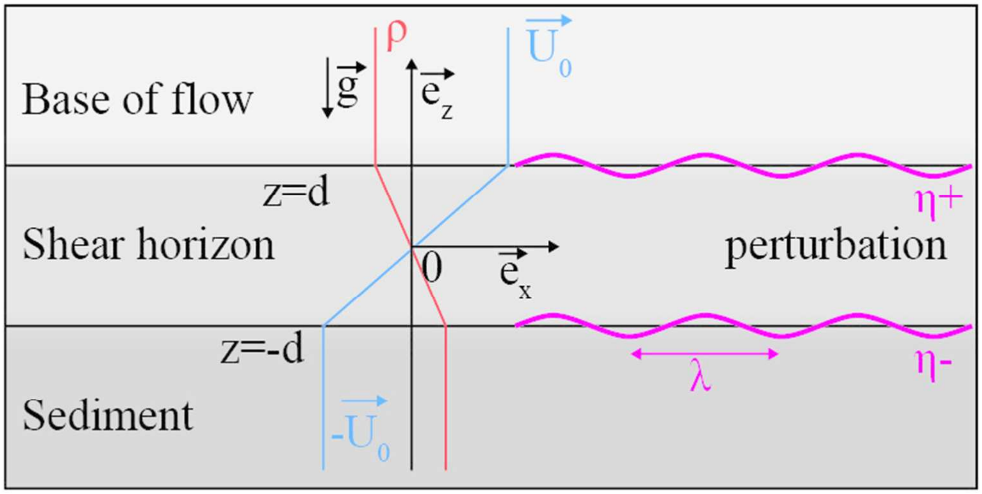

Figure 12: Geometry of the physical framework.

70x35mm (300 x 300 DPI)

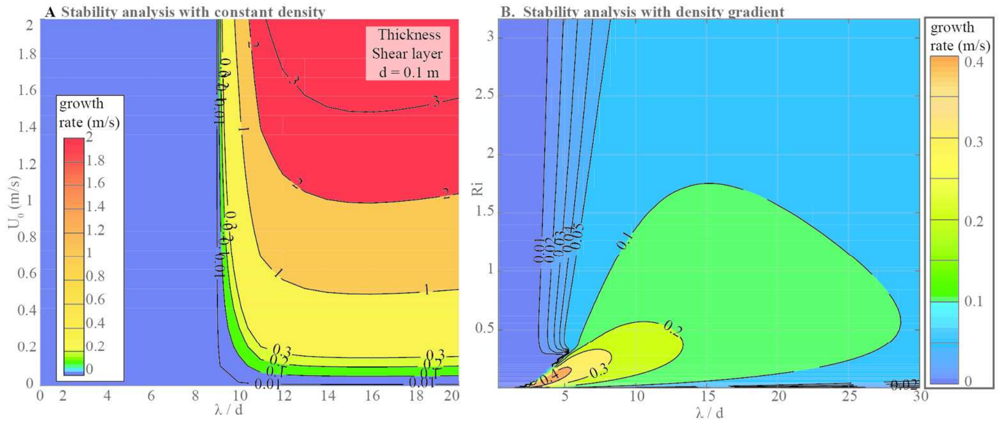

Figure 13: Results of the stability analysis from the physical frameworks with the constant density model (A), and linear density gradient (B), with zoom, showing the growth rate of the perturbation as a function of flow velocity (A) or Richardson number (B) and the ratio of wavelength over thickness of shear layer.

180x77mm (300 x 300 DPI)

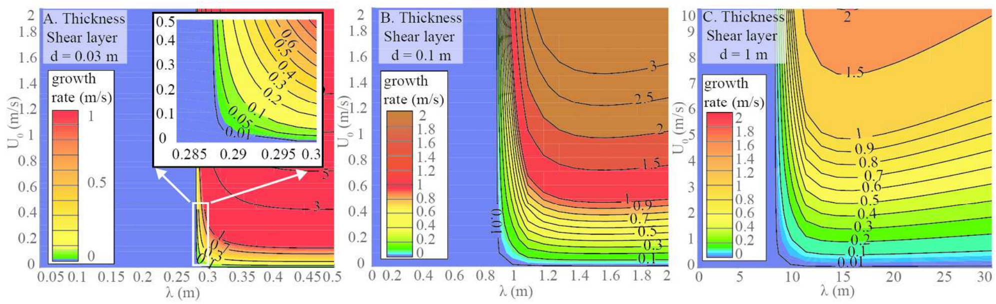

Figure 14: Constant density model. Growth rate of the perturbation as a function of wavelength and flow velocity for different thicknesses of shear layer. Case A is most relevant to the Tungurahua shark-fins.

180x54mm (300 x 300 DPI)

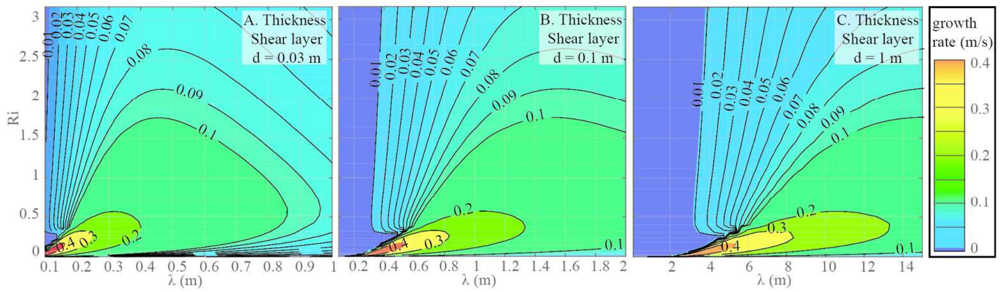

Figure 15: Gradient density model. Growth rate of the perturbation as a function of Richardson number and wavelength for different thicknesses of shear layer. Case A is most relevant to the Tungurahua shark-fins.

180x53mm (300 x 300 DPI)

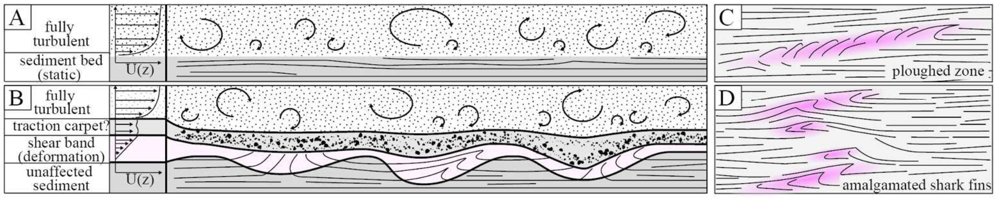

Figure 16: Interpretative sketch representing the process of formation of shark-fins. (A) In a regular setting, a fully turbulent boundary layer is developed down to the substrate. (B) If a basal granular flow is present in the form of a thin traction carpet, a shear horizon occurs, which reworks the superficial bed and creates shark-fins when the interface becomes wavy.

180x34mm (300 x 300 DPI)

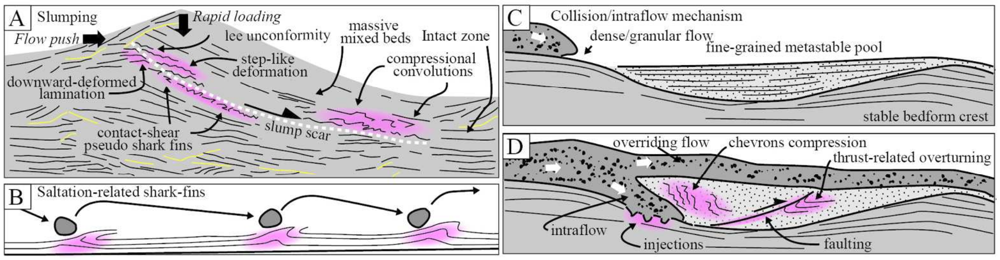

Figure 17: Interpretative sketches for the alternative explanations. A) the slumping mechanism for the lunate outcrop. B). In-train shark-fins might be related to the impact of saltating gravels. C) and D) The mechanism of collision forming the crocodile mouth via the flow of a dense granular flow over a fine-grained, metastable "pool".

180x46mm (300 x 300 DPI)

Plate set		Affected zone			Overlying beds:	Overturned structure:					Upper		Lateral continuity			Position		
Type	Plate	Slo (°)	Fac	GS & strat range	GS & strat	L (cm)	T (cm)	N	E (cm)	D- (cm)	Slop (°)	Type	upstream	downstream	comments	vert (cm)	hor (cm)	seq.
LunateT2																		
Truncated R-crest	LuT2P2	-30	C	fin L	fin to mid L	5	0.5	>20	0,7	55	10	ER	crest	disturbed zone		60	36	M
Convol	LuT2P2	-35	L	mid DL	fin to mid L	4	1.5	12	1	11	-15	C	truncated-R-crest	long DIST lens -local		63	26	M
Truncated F-crest	LuT2P2	-30	C	fin L	fin to mid L	2	0.4	3	0,5	/	0	ER	crest w. trunc.	Convol		58	32	M
Convol	LuT2P2	-30	L	fin to mid CL	fin DIST	12	2.5	20	1.5	13	-20	C	SOT crest	diffuse shear zone	prox. to crest	62	18	M
Convol	LuT2P2	-35	L	fin to mid DL	fin DIST	6	1	10	1,3	42	-30	C	steep trunc.	disturbed zone	base of shear band	72	31	M
chaotic Convol	LuT2P3	-30	L	fin to mid DIST	fin DIST	9	5	NV	1.5	22	-30	C	disturbed zone	disturbed zone	coa lens above	73	49	M
chaotic Convol	LuT2P3	-25	L	fin to mid DIST	fin to mid DIST	20	3	NV	>2	75	-20	C	disturbed zone	disturbed zone	coa lens above	79	22	M
chaotic Convol	LuT2P4	-15	L	mid to coa DIST	fin coa L	14	4	NV	>3	40	0	C	lapilli intercalated	concordant	lapilli intercalated	75	6	M
chaotic Convol	LuT2P5	-10	L	fin to mid DIST	fin to mid L	9	4	NV	3,5	18	0	C	disturbed zone	disturbed zone		62	25	M
chaotic Convol	LuT2P5	-10	L	fin to mid DIST	fin to mid L	9	3	NV	3	/	0	C	disturbed zone	disturbed zone		62	12	M
fluid escape ?	LuT2P2	-20	L	fin to mid DL	fin to mid L	2	3	12	/	/	/	/	massive zone	massive zone	might be shark fin	91	31	M
Truncated R	LuT2P3	-15	L	fin DL	mid to coa CL	6,5	1.2	>20	0.5		0	ER	lensoidal trunc.	concordant		102	13	M
Truncated R	LuT2P3	-15	L	fin L	fin L W	5	0.9	7	1,5		5	ER	BCKS rip.	wavy concordant		154	26	B
SOT	LuT2P3	-15	L	fin CL	coa M	14	0.7	16	0.8	22	55	ER	planar trunc.	continuity w. shear zone	covered by coa lens	143	16	B
Convol	LuT2P4	-15	L	fin CHAOS	fin DL	2	0.5	2	0.3	18	-10	C	fin DL shear band	fin DL shear band		108	42	B
Convol	LuT2P4	-15	L	fin CHAOS	fin DL	2	0.5	2	0.3		-10	C	fin DL shear band	fin DL shear band	linked with next? (at lower strat height)	113	23	B
Convol	LuT2P4	-20	L	fin DIST	fin DIST	5	1.5	8	1,5	12	0	C	shear plane	sub-planar shear plane	compound shark fins	116	27	B
Convol	LuT2P4	-20	L	fin DIST	fin DIST	4	1.4	3	1,6	30	0	C	shear plane	sub-planar shear plane		117	17	B
Convol	LuT2P5	-10	L	fin to mid L	fin DL	4	1.6	8	1.5	/	0	ER	shear plane	sub-planar trunc.		105	42	B
chaotic Convol	LuT2P6	-10	L	mid to coa DIST	fin coa DIST	10	3	NV	3,5	26	-5	C	long DIST. band	chaotic zone	highly deformed	42	39	M
chaotic Convol	LuT2P6	-5	L	fin coa DIST	fin CL	10	5	NV	2,5		0	C	long DIST. band	chaotic zone	thick disturbed zone	45	14	M
Convol	LuT2P3	-15	L	fin DL	fin DL	5	1.1	16	1,1	5	-5	C	trunc. by BCKS rip.	trunc. by BCKS rip.		150	28	B
Convol	LuT2P3	-15	L	fin DL	fin DL	2	0.8	6	0,5		-5	C	trunc. by BCKS rip.	trunc. by BCKS rip.		151	23	B
Truncated R	LuT2P4	-15	L	fin CL	fin CL	1.5	0.5	8	1	/	25	ER	erosive lense	planar trunc.		122	22	B
chaotic Convol	LuT2P5	-10	L	fin coa DIST	fin coa DIST	12	4.5	NV	3	/	0	C	between 2 chaotic	concordant		52	38	M
fluid escape ?	LuT2P5		F	fin DL CHAOS	fin CHAOS coa CHAOS	5	2	>16	1	/	0	C	between 2 chaotic	between 2 shear zones	base of shear band	51	11	M
Convol	LuT2P6	-15	L	fin CL coa CL	mid M coa M	2	1	3	1	/	0	C	shear zone	shear zone	strong GS interface	35	16	M
sub-vert. trunc	LuT2P6	-10	L	fin DL	mid DL	5		X		/	75	ER	sub-vert. trunc train	shear zone		75	49	B
Convol	LuT2P6	-10	L	fin DL	fin coa L	7	1.1	11	1,5	18	0	C	sub-vert. trunc	continuity w. truncated-R	below coa lens	72	30	B
Truncated R	LuT2P6	-10	L	fin DL	fin DL	5	0.5	7	0,5	11	0	ER	continuity w. convol.	NV		76	19	B
LunateT3																		
Convol	LuT3P1	-15	L	fin DIST mid DIST	fin to mid CL	4	2	>5	0.8	12,5	-10	C	sub-H trunc.	concordant	ploughed zone?	56	17	M
Convol	LuT3P1	-15	L	fin DIST mid DIST	fin to mid CL	3	1.5	>5	1.5	/	-15	C	sub-H trunc.	concordant	ploughed zone?	56	9	M
Convol	LuT3P1	-15	L	fin DIST mid DIST	fin to mid CL	3,5	1.5	>3	0.5	6.5	-15	C	sub-H trunc.	concordant	ploughed zone (21 cm long)	55	36	M
Convol	LuT3P1	-15	L	fin DIST mid DIST	fin to mid CL	3	1.5	>3	1	/	-15	C	sub-H trunc.	concordant		56	21	M
Truncated R	LuT3P1	-5	F	fin CL	fin to mid CL	5	1	x	1	26	5	ER	sub-H lam.	sub-H trunc.		104	10	B
Truncated R	LuT3P2	-10	L	fin CL	fin to mid CL	3	0.5	x	0,8	/	0	ER	sub-H trunc.	concordant	at stratigraphic break in slope	140	36	B
Truncated R	LuT3P1	-5	F	fin to mid CL	fin to mid CL	3	1	9	0.5		-10	ER	sub-H trunc.	sub-H trunc.	unclear struct.	102	23	B
Convol	LuT3P2	-5	L	fin to mid DIST	fin CL	4	0.7	6	2.5	6	0	C	trunc. by SOT	shear band	injectite?	44	23	M
Convol	LuT3P2	-5	L	fin to mid CL	fin CL	5	1	6	1	6	0	C	shear band	shear band		45	21	M
Convol	LuT3P2	-5	L	fin CL	fin CL	6	2	9	2	6.5	0	C	shear band	shear band		43	11	M
Truncated R	LuT3P2	-5	L	fin CL	fin CL	3	0.7	11	0.5	/	5	ER	shear band			43	4	M
Truncated F	LuT3P2	-5	L	fin DIST	fin to mid CL	10	0.7	x	0,6	/	10	ER	NV	concordant		77	13	M
Convol	LuT3P2	-15	L	fin to mid DIST	mid CL	6	1	>3	0,8	31	-10	C	concordant	concordant	2 compound structures	98	39	M
Convol	LuT3P2	-15	L	fin to mid DIST	mid DL	9	2	6	1.3	/	0	C	concordant	concordant	presence of lapilli clasts	104	6	M
Truncated F	LuT3P3	-20	L	fin to mid CL	fin DL	15	1	>20	1	/	5	ER	steep trunc. (35°)	surface		5	25	T
Convol	LuT3P3	-15	L	fin DIST	fin DL	2	1	7	0.6	/	-15	C	concordant	sub-planar trunc.		32	32	M
Truncated R	LuT3P3	-5	L	fin CL	fin CL	3	0.5	9	0.3	/	0	ER	sub-H trunc.	sub-planar trunc.		53	28	M
Truncated R	LuT3P3		F	fin CL	fin to mid CL	2	1.5	7	0,4	20	20	ER	eros. gullie	trunc. in DIST. zone	produces a bump	58	9	M
Truncated R	LuT3P4		F	fin DIST	fin DL	3	0.6	5	0,6	10	5	ER	sub-H trunc.	sub-planar trunc.	broad & thick deformed zone	38	45	M
Convol	LuT3P4	-15	L	fin DL	fin CL	4	1	5	0,5	12	-15	C	shear band	shear band	broad & thick deformed zone	38	35	M
Truncated R	LuT3P4	-15	L	fin CL	fin CL	3	0.8	7	0,5	37	0	ER	sub-H trunc.	sub-planar trunc.	broad & thick deformed zone	38	23	M
Convol	LuT3P5	-20	L	fin DIST	fin CL	7	1.5	>5	1,2	35	-5	C	sub-planar trunc.	sub-planar trunc.	2 compound structures	30	41	M
Convol	LuT3P5	-15	L	fin DIST	fin cr	5	1.5	>9	1	19	-10	C	sub-planar shear	sub-planar shear		40	8	M
Convol	LuT3P6	-20	L	fin DL	fin CL	5	1.8	>3	1,2	/	-20	C	sub-planar shear	concordant		34	44	M
Convol	LuT3P3	-10	L	fin DL	fin to mid CL	7	2.5	?	1	21	0	C	NV	sub-planar shear		68	8	M
Convol	LuT3P4	-15	L	fin to mid DIST	fin to mid CL	3	1	7	0.5	5	-10	C	sub-planar shear	sub-planar trunc.		53	42	M
Convol	LuT3P4	-15	L	fin to mid DIST	fin to mid CL	3	1	7	0.5	75	-10	C	sub-planar shear	sub-planar trunc.		53	37	M
Convol	LuT3P5	-15	L	fin to mid CL	fin CL	3	1.5	8	1	38	0	C	concordant	BCKS rip.	2 compound structures	53	18	M
Convol	LuT3P6	-15	L	fin to mid CL	coa mid M	9	2.3	12	2	/	0	C	sub-planar shear	No shear, fin to mid CL		48	32	M
Truncated F-crest	LuT3P3	-12	L	fin to mid CL	fin to mid DL	14	1	>20	0,7	/	12	ER	sub-H trunc.	crest		67	32	M
Convol	LuT3P3		F	fin DL	fin CL	>6	1.5	6	?	23	0	C	sub-H trunc.	deformed lense		77	35	M
Convol	LuT3P3	-15	L	fin DL	fin M	4	1.5	>3	0,8	25	0	C	smooth undulations	sheared length		83	10	M
Convol	LuT3P4	-15	L	fin to mid DIST	fin to mid CL	10	2.5	>9	2	17	-10	C	sub-planar shear	sub-planar shear	40 cm long shear band	68	43	M
Convol	LuT3P4	-15	L	miden DL	mid M	5	1.5	>3	0,5	52	0	C	sub-planar shear	ploughed zone	presence of lapilli clasts	67	23	M
Stepa	LuT3P4		L	fin DL	fin to mid DL	5	1	5	/	/	15		highly deformed	sub-H lam.	in relation with shark fins?	71	13	M
Convol	LuT3P5	-15	L	fin to mid DIST	fin to mid DL	3	1.5	3	>1	48	-10	C	block (5 cm diam.)	compound struct.		56	25	M
Convol	LuT3P6	-15	L	fin to mid DL	fin DL	10	3.5	>13	1	/	0	C	ploughed zone	shear zone		60	30	M
Convol	LuT3P4	-10	L	fin to mid CL	mid DL ploughed	6	2.7	19	1,5	/	15	C	BCKS rip.	concordant	2 compound convol.	32	41	M
Truncated R-crest	LuT3P3	-20	L	fin to mid CL	fin to mid CL	>10	2	>20	3,5	41	0	ER	sub-H trunc.	crest		103	36	M
Convol	LuT3P4	-20	L	fin DL	mid DL	3.5	1.5	9	1	6	0	C	crest w. OTF	sub-planar shear		84	47	M
Convol	LuT3P4	-20	L	fin DL	mid DL	3.5	1.5	9	1	56	0	C	crest w. OTF	sub-planar shear		84	43	M
Convol	LuT3P5	-15	L	fin to mid DL	fin to mid CL	10	2	>7	1.5	/	0	C	undul. trunc.	undul. trunc.		81	38	M
Truncated R	LuT3P4	-20	L	fin CL	mid M	7	0.5	7	0,6	/	-5	ER	sub-planar trunc.	sub-planar trunc.	within an erosive lens	120	28	B
Convol	LuT3P4	-15	L	fin to mid DIST	fin CL	7	2	>10	2	/	-15	C	coa grained horizon	NV		128	22	B
Convol	LuT3P5	-20	L	fin to mid DL	fin to mid DL	8	2.5	16	0.5		-5	C	concordant	concordant ploughed	angular	21	41	M
Truncated R	LuT3P6	-20	L	fin DL	fin CL	2	0.5	7	0.5	/	0	ER	7 cm block, BCKS rip.	shear band		93	45	B
LunateT4																		
Sub-vert. trunc.	LuT4P1	5	S	fin L	mid M	29	/	/	/	8	85	ER	splay & fade	Eroded 2 cm below surface		42	7	M
SOT crest	LuT4P2a	-20	S	fin DIST	fin mid M	>28	4	>20	2.5	30	45	ER	re incised by sub-vert.	Eroded 2 cm below surface		10	35	T
Convol crest	LuT4P2a	-20	L	fin DIST	fin mid DL	>4	>1.5	18	0.9	/	-40	ER	crest	DIST zone		10	22	T
Convol	LuT4P1	-20	L	mid coa M	mid coa M	5	2.5	13	2	47	-20	C	NV	coa M zone		75	36	B
Convol	LuT4P2	-25	L	mid coa M	fin DIST	7	2.5	NV	2.5	17	-25	C	coa M zone	coa M zone		81	41	B
Convol	LuT4P2	-25	L	mid coa M	fin DIST	7	2	NV	1.7	/	-25	C	coa M zone	coa M zone		87	27	B
Convol crest	LuT4P1a	-15	L	fin mid DL	fin mid L	9	3	13	1	16	-10	C	low angle erosion	fin DIST zone	2 compound duplex convol. -angular	80	6	M
Convol	LuT4P2	-20	L	mid DL	fin PLOUGHED	6	2	7	0.9	12	-20	C	crest	fin DIST zone		72	42	M
Convol	LuT4P2	-25	L	fin mid L	fin PLOUGHED	3	1	5	1	/	-25	C	crest	fin DIST zone		76	36	M
Truncated R-crest	LuT4P2	-20	L	fin DL	fin mid L	7	1	NV	0.3	13	-5	ER	crest	undul. shear		69	17	M
Truncated R	LuT4P2	-20	L	fin DL	fin mid L	7	1	8	0.3	15	-5	ER	crest	undul. shear		74	5	M
Convol	LuT4P3	-10	L	fin mid DL	fin mid L undul.	11	3.5	9	4	9	-15	ER	undul. shear	undul. shear	local slump ?	59	43	M
Convol	LuT4P3	-10	L	fin mid DL	fin mid L undul.	6	2	8	2	/	-15	ER	undul. shear	undul. shear		62	34	M
Convol	LuT4P3	-15	L	mid L	mid L undul.	4	1.7	8	0.7	6	0	C	deformed beds	undul. lam.	angular VL	70	39	M
Convol	LuT4P3	-20	L	fin mid DL	mid L undul.	>3	1	6	1	24	0	C	undul. lam.	undul. lam.	angular VL	74	33	M
Convol	LuT4P3	-10	L	fin mid DL	mid L undul.	7	1.8	>8	>1.5	/	0	C	undul. lam.	Bloc (>8cm) lense	2 compound duplex VL	80	9	M
sheared crest	LuT4P2a	-20	L	fin DL DIST	fin DL DIST	14	1.5	>8	NV	4	0	ER	erosion	sheared zone	sheared crest zone	12	33	T
Convol	LuT4P2a	-20	L	fin DIST	fin mid DL	>6	1.5	8	1.3	10	-20	C	crest	sheared zone	compound crest zone seems fluidized	15	16	T
Convol	LuT4P2a	-20	L	fin DIST	fin mid DL	3	0.8	>3	1.1	4	-20	C	crest	sheared zone		18	6	T
Convol	LuT4P3	-20	L	fin mid DIST	fin mid CL BCKS	4	>2	6	0.8	58	-20	C	crest	sheared zone		4	46	T
Convol	LuT4P3	-30	L	mid coa L	fin DIST	3	1.4	6	1.1	4	-20	C	crest	sheared zone		9	40	T
Convol	LuT4P3	-30	L	mid coa L	fin DIST	5	1.8	8	3	48	-20	C	crest	BCKS rip.	angular vl	9	36	T
Convol	LuT4P4	-25	L	fin DIST	fin L BCKS	4	1	>5	1.4	20	-20	C	BCKS rip.	local slump ?		10	40	T
Convol	LuT4P4	-25	L	fin DL DIST	fin DIST BCKS rip.	>10	NV	NV	NV	6	-15	C	sheared band	sheared band	local slump ?	16	20	T
Convol	LuT4P4	5	L	fin DL DIST	fin BCKS rip.	3	NV	14	NV	/	5	C	sheared band	BCKS rip.		18	14	T
Truncated R-crest	LuT4P2	-20	L	fin DL	fin mid L	7	1	NV	0.3	13	-5	ER	crest	undul. shear		69	17	M
Truncated R	LuT4P2	-20	L	fin DL	fin mid L	7	1	8	0.3	15	-5	ER	crest	undul. shear		74	5	M
Convol	LuT4P3	-10	L	fin mid DL	fin mid L undul.	11	3.5	9	4	9	-15	ER	undul. shear	undul. shear	local slump ?	59	43	M
Convol	LuT4P3	-10	L	fin mid DL	fin mid L undul.	6	2	8	2	/	-15	ER	undul. shear	undul. shear		62	34	M
Convol	LuT4P5	-20	L	fin DL DIST	fin mid CL	NV	NV	NV	NV	17	-10	C	crest BCKS	sheared or local slump ?	crest-related structure?	10	46	T
Convol	LuT4P5	-15	L	fin DIST	coa DL	5	1.5	12	1	/	-15	C	crest BCKS	sheared or local slump ?		12	29	T
Convol	LuT4P3	-15	L	fin mid CL	fin BCKS rip.	3	1	6	0.7	26	-15	C	erosion disturb	BCKS rip.		65	34	M
Convol	LuT4P3	-20	L	fin mid DL	fin L	5	1.5	9	1	/	-20	C	BCKS rip.	concordant		69	9	M
Truncated F crest	LuT4P3	-15	L	fin mid DL	fin mid DL	2	0.3	6	0.7	14	-5	ER	Low angle crest	disturb		48	31	M
Convol	LuT4P3	-15	L	fin mid DL	fin mid DL	5	1.5	NV	1	/	-15	C	Low angle crest	disturb		53	17	M
Convol	LuT4P3	-15	L	fin mid DL	fin L DIST	4.5	1.4	5	1.3	7	-10	C	BCKS rip.	shear zone		25	40	T
Convol	LuT4P3	-15	L	mid CL	fin L DIST	4	2.5	4	1.4	12	-10	C	shear zone	shear zone		26	31	T
Convol	LuT4P3	-15	L	fin DL	fin L DIST	9	2.7	NV	2.9	18	-10	C	shear zone	shear zone		27	24	T
Convol	LuT4P3	-15	L	fin DL	fin L DIST	8	2.4	9	2.1	/	-10	C	shear zone	Lee trunc.		28	12	T
Convol	LuT4P4	-20	L	fin mid DL	fin mid CL undul. BCKS	7	3.3	>8	1.3	13	-25	ER	BCKS rip.	undul. lam.		24	45	M
Convol	LuT4P4	-20	L	fin mid DL	fin mid CL undul. BCKS	5	2	NV	1.5	/	-25	ER	undul. lam.	long trunc.		29	34	M
Truncated R	LuT4P3	-20	L	fin L	fin mid CL	3	1.5	13	1	22	0	C	concordant well lam.	undul. BCKS		28	44	M
Convol	LuT4P3	-20	L	fin mid DL	fin L undul. BCKS	3	1	7	1	/	0	C	undul. BCKS	low angle undul.		32	23	M
Truncated R-crest	LuT4P4	-20	L	fin mid CL	fin mid DL BCKS rip.	6	1.5	9	0.8	8	+5	ER	erosive BCKS lens	undul. trunc.		38	42	M
Convol amalgam	LuT4P4	-20	L	fin mid DL	fin mid DIST	6	2	NV	>1	27	-20	C	undul. trunc.	ploughed	very local crest from BCKS	38	34	M
Truncated R	LuT4P4	-20	L	fin mid DL	fin mid CL BCKS rip.	6	1.6	8	1.4	/	-10	C	ploughed	ploughed		45	7	M
Truncated R	LuT4P4	-5	L	fin L	mid BCKS rip.	7	2	>7	1	9	5	ER	carbonised branches	shear zone	local crest	98	23	B
Convol	LuT4P4	-5	L	fin L	mid BCKS rip.	4	1.2	5	0.5	/	0	C	shear zone	concordant, steepens to -25°		98	14	B
Convol	LuT4P5	-20	L	fin DIST	fin DL	10	2.3	12	3	/	-20	C	BCKS rip. crest	low angle BCKS	angular thrust	12	21	T
Truncated R	LuT4P5	-15	L	fin DL	fin mid DL	9	1.5	9	0.5	8	-10	ER	low angle trunc.	shear zone		47	14	M
Convol	LuT4P5	-15	L	fin DL	fin mid DL	3	1	NV	0.7	/	-5	C	shear zone	concordant shear zone		49	7	M
Convol	LuT4P5	-20	L	fin DL DIST	fin L	4.5	1	NV	0.5	4.5	-20	C	sub planar trunc.	shear zone		44	35	M
Convol	LuT4P5	-20	L	fin DL DIST	fin L	4.5	1	NV	0.5	58	-20	C	shear zone	shear zone		40	37	M
Convol	LuT4P5	-20	L	fin DL DIST	fin L	4.5	1	NV	0.5	5.5	-20	C	shear zone	shear zone		35	38	M
Convol	LuT4P5	-20	L	fin DL DIST	fin L	4.5	1	NV	0.5	4	-20	C	shear zone	shear zone		31	40	M
Convol	LuT4P5	-20	L	fin DL DIST	fin L	4.5	1	NV	0.5	5	-20	C	shear zone	shear zone		26	42	M
Convol	LuT4P5	-20	L	fin mid DL DIST	fin L	4.5	1	NV	0.5	13	-20	C	shear zone	shear zone		45	13	M
Convol	LuT4P5	-20	L	fin mid DL DIST	fin L	4.5	1	NV	0.5	5	-20	C	shear zone	shear zone		48	8	M
Convol	LuT4P6	-20	L	fin mid DL DIST	fin L	4.5	1	NV	0.5	/	-20	C	shear zone	low angle trunc.		42	45	M
Convol	LuT4P5	-20	L	fin mid L	fin mid DL	7	3	10	1.2	/	-20	ER	low angle trunc.	impact sag?	compound & angular VL.- impact zone?	57	29	M
Truncated R	LuT4P6	-15	L	fin mid CL	fin mid CL	3	1	12	0.5	/	0	ER	low angle BCKS	low angle BCKS		25	42	M
Truncated R	LuT4P6	-15	L	fin DL	fin mid DL	3	1	8	NV	/	-10	ER	sub-H trunc. fin BCKS	concordant		32	40	M
Truncated R	LuT4P6	-25	L	fin CL	fin undul BCKS	2	0.5	8	0.3	/	-15	ER	low angle BCKS pool	low angle BCKS pool		7	42	T
TransverseT1A																		
Convol	TrT1aP1	-20	L	fin DIST	fin to mid CL	>8	1.8	6	1,8	21	-10/	ER/	undul. lam.	H trunc. w. truncated-R	thick laminated	85	9	B
Truncated R	TrT1aP2	-15	L	fin to mid d	fin to mid CL	7,5	1	4	2,3	72	-10	ER	sub-H trunc. w. VL	sub-planar trunc.	thick sheared lam.	110	44	B
Truncated R	TrT1aP3	-5	L	fin to mid DIST	fin CL	2,2	0.7	8	0,7	/	0	ER	shear lense	planar trunc.		123	26	B
Convol	TrT1aP1	-20	L	fin DIST	fin CL	5	4	>20	1	20	-20	C	horizontal part of sub-	shear zone	crest-related structure?	36	1	M
Convol	TrT1aP2	-20	L	fin DIST	fin to mid CL	>5	3	>20	2	9.5	-15	C	shear zone	ploughed zone		64	46	M
Convol	TrT1aP2	-20	L	fin DIST	fin to mid CL	5	2	10	0,7	/	-15	C	shear zone	shear zone		65	34	M
Steps	TrT1aP1	-15	L	fin DL	fin M	5	0.5	3	/	/	-15	conc	NV			78	46	B
Truncated R	TrT1aP2	+5	C	fin DIST	fin DL	7	1.8	12	1,7	7	20	ER	truncated by sub-vert.	duplex shear zone	crest-related structure?		39	T
Truncated R	TrT1aP2		C	fin DIST	fin DIST	8	1.8	10	1.5	21	15	ER	truncated by sub-vert.	undul. shear plane	shear band	35	33	T
Truncated R	TrT1aP2		F	fin DL	fin to mid L	3	0.4	4	0,5	/	5	ER	undul. shear plane	eros. based BCKS rip.		34	8	T
Convol	TrT1aP2	-25	L	fin CHAOS	fin to mid CL	46	2	X	1	/	-25		shear zone	shear zone	45 cm long sheared zone	51	44	M
deformation	TrT1aP2	-25	L	fin CHAOS	fin to mid CL	46	2	X	1	/	-25		shear zone	shear zone	45 cm long sheared zone	71	44	M
Convol	TrT1aP3	-15	L	fin DIST W-BCKS	mid CL	>8	3	17	1,4	13	-15	C	major sub-H trunc.	shear zone	thick shear zone	48	43	M
Convol	TrT1aP3	-15	L	fin DIST W-BCKS	fin L	9	1.8	12	0,9	45	-15	C	major sub-H trunc.	shear zone	thick shear zone	49	30	M
Truncated R	TrT1aP4	-10	L	fin DL	fin to mid DL	5	1.2	12	1	15	-10	ER	shear zone	shear zone	Single eros. plane produces 3 truncated-R	43	40	M
Truncated R	TrT1aP4	-10	L	fin DL	mid M	4	0.9	12	0.5	16	-10	ER	shear zone	shear zone	Single eros. plane produces 3 truncated-R	44	24	M
Truncated R	TrT1aP4	-10	L	fin to mid DL	mid M	10	1.3	16	2	42	-10	ER	shear zone	shear zone	Single eros. plane produces 3 truncated-R	48	8	M
Truncated R	TrT1aP5	-10	L	fin DL	mid M	12	0.7	16	1	/	-10	ER	shear zone	possibly ploughed zone	eros. plane evolves into shear band	43	16	M
Truncated R	TrT1aP3	-15	L	fin DL	fin to mid W-BCKS	>5	1.1	>10	1,5	43	-10	ER	W-BCKS rip.	chaotic zone	DIST and ploughed?	53	49	M
Truncated R	TrT1aP3	-20	L	fin W-BCKS	fin CHAOS	>10	3.5	>20	2,5	/	30	ER	chaotic zone	BCKS rip. zone	thick DIST zone	62	4	M
Truncated R	TrT1aP3	+5	L	fin DL	fin DL	5	1	14	1,5	0	0	ER	BCKS rip. zone	trunc. vanish on shear zone		72	16	M
chaotic zone	TrT1aP3	-10	L	fin to mid CHAOS	ondulating BCKS	87	6	NV	NV	87	5	C	shear band	trunc. BCKS-rip.		73	14	M
chaotic zone	TrT1aP5	-10	L	fin to mid CHAOS	ondulating BCKS	87	6	NV	NV	20	5	C	shear band	trunc. BCKS-rip.		62	38	M
Convol	TrT1aP5	-15	L	fin DIST	mid M	5,5	1.5	10	1,9	/	-15	C	sub-vert. trunc trunc.	vanish	trunc. but correlable w. long chaotic lens	63	18	M
Truncated F	TrT1aP5	-15	L	fin to mid CL	mid DL	6	0.3	8	0,4	/	-5	ER	undul. trunc.	undul. trunc.		56	44	M
Convol	TrT1aP6	-15	L	fin DL	fin DL	3	0.5	6	0.5	11	0	ER	major sub-H trunc.	concordant		5	34	T
Truncated R	TrT1aP6	-15	L	fin DL	fin DL	4	0.5	6	0,3	/	0	ER	major sub-H trunc.	concordant		5	17	T
Convol	TrT1aP6	-25	L	fin DL mid DL	fin CL	2	0.5	3	0.5	12.5	-15	C	fin shear band	BCKS zone		37	34	M
Truncated R	TrT1aP6	-25	L	fin CHAOS mid	mid DL	8	2.5	>10	4	/	-15	C	fin shear band	BCKS zone	Thick deformation zone	44	17	M
Truncated R	TrT1aP6	-15	L	fin DL	fin to mid CL	5	0.4	15	1	/	0	ER	undul. trunc.	undul.		62	14	M
TransverseT1B																		
fluid escape?	TrT1bP2	-15	L	fin CHAOS	fin DL								sub-H trunc.	sub-H trunc.		57	44	M
Convol	TrT1bP2		F	fin to mid DIST	fin CL	3	1.5	8	1		-5	C	coa gullie	major H trunc.	may be the cast of a large clast	65	13	M
Convol	TrT1bP3	-10	L	fin L	coa M	4	1.1	NV	1,3	62	-10	C	coa lens	base of bedform		23	11	M
Truncated R	TrT1bP5	-5	F	fin CL	mid M	3	0.5	5	0,7	/	5	C	coa lense/layer	sub-H trunc.		35	48	T
Truncated R	TrT1bP6	-15	L	fin to mid CL	mid M	7	1	20	0.5	20	20	C	sub-H trunc.	sub-H trunc.		67	30	M
Convol	TrT1bP6	-15	L	fin to mid CL	fin to mid CL	9	1.5	24	1,9	/	0	C	ploughed lense	NV	/	68	10	M
Convol	TrT1bP6	-15	L	fin DL	fin CL	7	1	18	1		0	C	truncated shear plane	concordant		70	45	M
TransverseT2																		
Convol-crest	TrT2P2	-5	L	fin ploughed	fin to mid CL	6	1	>3	1	24	-20	C	crest zone	shear band		80	12	M
Convol	TrT2P3	-20	L	fin to mid CL	fin to mid DL	3,5	2	10	1	21	-20	C	shear band	shear band		100	40	M
Convol	TrT2P3	-25	L	fin ploughed	fin to mid CL	9	3	>17	1	11	-20	C	shear band	shear band	Thick deformation zone, underlying coa layer	105	22	M
Convol	TrT2P3	-25	L	fin ploughed	fin to mid CL	4	2	>5	1,3	12	-20	C	shear band	shear band		109	11	M
Truncated F	TrT2P4	-15	L	fin L	fin CL	3	0.5	>8	0.8	32	-5	ER	shear band	conforme		91	49	M
sub-vert. trunc	TrT2P4	-20	L	fin to mid CL	mid DL BCKS	6				/	40	ER	shear plane	sub-planar trunc.	sub-vert. trunc at downstream end of train	102	14	M
Convol	TrT2P3	-5	L	fin CHAOS	fin CL mid M	3	1.5	6	1,1	4	5	C	sub-H trunc.	shear plane	injectite?	75	29	M
Convol	TrT2P3	-5	L	fin CL	fin L	4	2	>10	1,4	6.5	5	C	shear plane	shear plane		75	24	M
Convol	TrT2P3	-5	L	fin DL	fin DL	6	1	>7	1	10.5	0	C	shear plane	shear plane	in duplex compound	77	20	M
Convol	TrT2P3	-5	L	fin CL	fin L	5	1.5	>11	0.7	19	0	C	shear plane	shear plane		76	10	M
Convol	TrT2P4	-5	L	fin to mid DL	fin to mid CL	5	1	>7	1,1	/	0	C	shear plane	sub-H trunc.		62	43	M
Convol	TrT2P3	-20	L	fin to mid DL	fin to mid CL	11	1.7	>3	1,5	10	-10	C	NV	shear plane	ploughed zone	133	37	B
Convol	TrT2P3	-20	L	fin to mid CL	fin to mid CL	4	1	>4	0,6	/	-10	C	shear plane	concordant fin cl	thick affected lam.	135	28	B
Truncated R	TrT2P4	-5	L	fin to mid DL	fin to mid DL	3	0.5	>4	0,9	/	10	ER	strange sharkfin	fading in massive		58	29	M
Convol	TrT2_P4		F	fin CL	fin CL	2.5	0.5	NV	0,4	/	-5	C	sub-planar trunc.	sub-planar trunc.		62	6	M
Truncated R	TrT2P5	-15	L	fin coa CL	fin coa CL	4	1.5	>8	0,7	/	10	ER	W-BCKS rip.	undul.	scoria block underneath	97	41	B
Truncated R	TrT2P5	-15	L	fin CL	fin to mid CL	5	1	7	0,6	/	0	C	sub-H trunc.	concordant undul.		89	33	B
Truncated F	TrT2P5	-25	L	fin to mid CL	fin to mid CL	11	4	18	0,6	19	-5	C	sub-H trunc.	deformation zone	compound, injectite?	39	41	T
Convol	TrT2P5	-25	L	fin to mid ploughed	fin ploughed	6	2.5	8	0,5	10	-15	C	downstr. limit of trunc.	ploughed zone		43	22	M
Convol	TrT2P5	-25	L	fin to mid CL	fin ploughed	7	3	20	1	48	-10	C	sub-H trunc. w.	shear zone	ploughed zone?	45	14	M
Convol	TrT2P6	-10	L	mid DL	fin to mid DL	3	1	5	0.6	/	-5	C	surface of a shear pool	surface of a shear pool	compound, ploughed zone?	37	22	M
Truncated R	TrT2P6	-20	L	fin CL	fin CL	≥ 2	0.5	8	0,6	/	O	ER	W-BCKS rip.	NV		59	1	B
creneaux	TrT2P6	?	?	fin DL mid DL	mid M	6	5	>20	/	/	?	?	sub-H trunc.	end of plate		73	9	B
TransverseT3																		
Truncated R	TrT3P2		F	mid CL	fin to mid CL	7	1	18	1	/	0	ER	sub-H trunc.	sub-H trunc.		172	25	B
Truncated F	TrT3P3		S	fin DL W	fin to mid CL	6	0.5	4	0,5	/	20	ER	straight trunc. (20º)	shear band		86	20	M
Truncated F	TrT3P3		C	fin to mid L	fin CL	6	0.5	X	>0,5	/	25	ER	straight trunc. (30º)	NV		14	4	crete
Truncated F	TrT3P3	15	S	fin CL undul.	fin CL W	7	0.6	>20	0,9	/	35	ER	undul. trunc. (ca. 25º)	undul. trunc.		97	10	M
Convol	TrT3P5	-35	L	fin to mid dt	coa M	12	2	>12	0,7	/	-35	C	crest area	fin M concordant lens	lapilli clasts in overlying zone	22	15	T
Truncated R	TrT3P5	-25	L	fin CL	fin CL	4	0.5	10	0,6	/	0	ER	H trunc.	concordant	lapilli clasts in overlying zone	34	23	M
Truncated R	TrT3P6	-10	L	fin CL	fin to mid CL	4	1	12	0.5	/	0	ER	shear plane w. VL	concordant fin cl		15	29	T
Convol	TrT3P6	-20	L	fin CL	fin CL	4	0.7	8	0,9	/			sub-H trunc.	concordant		22	16	M
Truncated R	TrT3P5		F	fin to mid dt	fin to mid DL	4	0.8	6	1	/	5	C	ploughed zone	concordant		59	28	M
TransverseT4																		
Truncated R	TrT4P1		F	fin CL	fin CL	3,4	0.4	>7	0,3	34	5	ER	wavy fin CL	BCKS rip.		128	20	B
Truncated R	TrT4P2		F	fin DL	fin CL	3	0.8	>2	0.5	/	10	ER	W-BCKS rip.	wavy climbing rip.		144	39	B
Truncated F	TrT4P1	-15	L	fin CL	fin to mid DL	>6	0.5	>13	2		0	ER	NV	sub-H trunc.		105	45	M
Convol	TrT4P1		F	fin CLimbing rip.	fin CL	2.5	0.5	4	0,5	30	0	C	weak planar trunc.	climbing rip.	compound	120	4	B
Truncated R	TrT4P2	-10	L	fin CL	fin CL	12	0.5	20	0,8	9	-5	ER	sub-H trunc.	shear climbing in strat.	base of shear band	135	23	B
Convol	TrT4P2	-10	L	fin L	fin L	3	0.8	13	0.5	/	0	C	climbing shear zone	shear climbing in strat.		135	17	B
Convol	TrT4P2	-15	L	fin L	fin to mid L	7	1	7	1,4	24	-15	C	major sub-H trunc.	shear zone	cluster of shark fins (vertically & laterally)	123	40	B
Convol	TrT4P2	-15	L	fin L	fin to mid CL	6	1	12	1,1	-5	-10	C	shear zone	BCKS rip.	climbing backward in strat with next	129	11	B
Convol	TrT4P2	-15	L	fin to mid CL	fin L	9	2.5	>15	1,9	8	-10	C	climbing shear zone	climbing shear plane		130	16	B
Truncated R	TrT4P2	-15	L	fin to mid CL	fin L	5	0.5	9	1	31	-10	ER	shear zone	concordant		130	10	B
Convol	TrT4P3	-20	L	fin DL	fin L	7	1	24	1	/	-10	C	climbing shear zone	climbing rip.		153	30	B
Truncated R	TrT4P3	-25	L	fin DL	fin CL tronqué par	4	0.7	>4	0.5	/	-15	ER	strange coarse lense	undul. trunc.		143	19	B
Truncated R	TrT4P4	5	S	fin to mid CL	fin to mid CL	4	1	>7	0,7	/	15	ER	low angle trunc.	wavy climbing rip.		52	40	M
Truncated R	TrT4P4	-20	L	fin to mid DL	fin CL	>4	1.8	10	1,3	/	-10	ER	low angle trunc. (-10)	NV		145	43	B
Truncated R	TrT4P4	10	S	fin to mid L	fin to mid CL	5	1.8	16	1	19	15	ER	undul. concordant	undul. concordant		56	30	M
Convol	TrT4P4	15	S	fin L	fin DL	2,5	1	7	0,4	20	15	C	undul. concordant	concordant cl	highly deformed zone	52	9	M
Truncated R-crest	TrT4P5	-30	L	fin to mid CL	fin to mid CL	6	0.5	>15	0,5	16	15	ER	truncated-R	crest coa lense		36	43	M
Convol	TrT4P5	-20	L	mid to coa DL	fin DL DIST	7	2	>4	1,5	13	-20	C	crest zone	disturbed lense	coarse VL local slump?	40	30	M
Convol	TrT4P5	-20	L	mid to coa DL	fin DL DIST	7	3	>4	2	30	-20	C	disturbed lense	disturbed fin lense	coarse VL local slump?	45	16	M
Convol	TrT4P6	-15	L	coa M	fin ploughed	14	3.5	>3	9 ou	37	-10	C	compound ploughed	compound ploughed zone	coarse VL local slump?	42	41	M
Convol	TrT4P6	-10	L	fin CHAOS	fin CL	6	1.5	>6	1,5	/	-5	C	compound ploughed	NV	coarse convol. local slump?	44	3	M
Truncated R-crest	TrT4P5	-30	L	fin to mid CL	fin to mid CL	4	0.3	6	0.5	/	10	ER	low-angle trunc.	concordant		41	41	M
Truncated R-crest	TrT4P5	-25	L	fin to mid CL	fin CL	6	0.6	9	0,6	/	0	ER	long low-angle trunc.	concordant planar		22	34	crête
Convol	TrT4P5	-20	L	fin DL	fin CL	3	1.2	5	0,8	9	-20	C	truncated by OTF	shear zone		44	41	M
Convol	TrT4P5	-20	L	fin DL	fin to mid CL	3,5	1.2	5	0,6	/	-20	C	shear zone	concordant		44	32	M
Convol	TrT4P5	-15	L	fin ploughed	fin CL	3	0.8	8	0,7	/	-5	C	ploughed "injected"	concordant	intrabed injectite?	60	8	M
Convol	TrT4P5	-20	L	fin to mid CL	fin to mid CL	4	1	6	NV	17	?	?	concordant lee	concordant lee	angular	44	0	M
Convol / Steps	TrT4P6	-20	L	fin to mid CL	fin to mid CL	>6	2	>8	1,1	12	-20	C	concordant lee	concordant lee	creneau	34	36	M
Convol angular	TrT4P6	-20	L	fin to mid CL	fin to mid CL	>6,5	2.2	>8	2	/	-20	C	concordant lee	concordant lee	angular	36	25	M
Truncated R-crest	TrT4P5	-20	L	fin L	fin CL	2,5	1	>5	0,7	39	-20	C	trunc. by BCKS rip.	concordant		85	23	B
Convol	TrT4P6	-10	L	fin L	mid to coa L	2,5	1.1	>5	0,6	/	-10	C	concordant	BCKS rip.		75	39	B
Truncated R-crest	TrT4P5	-20	L	fin to mid DL	fin to mid CL	16	0.7	>16	1,5	15	0	ER	long low-angle trunc.	low angle concordant	at crest summit	100	0	B
Convol angular	TrT6P6	-20	L	fin to mid DL	fin to mid DL	2	0.8	6	0.5	13	-15	C	concordant	concordant				
Convol angular	TrT6P6	-15	L	fin to mid DL	fin to mid DL	2.5	1.2	NV	1.7	/	-10	C	concordant	NV		90	25	B

Annex 2

Stability of a wavy interface at a shear horizon

1. Setting

1.1. Initial configuration

The problem is considered in 2 dimensions (the vertical $\mathbf{e_z}$ and the horizontal flow direction $\mathbf{e_x}$). Two semi-infinite, incompressible fluids of constant velocity $\mathbf{U_0}$ are linked by a shear horizon of thickness *2*d* centered around *z=0* with linear velocity profile such as (Fig 12):

$$\overline{\boldsymbol{U_x}(z)} = \begin{cases} U_0 \;\; if\; z > d \\ -U_0 \;\; if\; z < -d \\ \frac{z}{d}.U_0 \; if\; |z| < d \end{cases} \qquad (1)$$

The mediums are considered incompressible and with density $\bar{\rho}(z)$, that is taken constant in one case (Chapter 2). In a second case, density is linearly decreasing with height and separated by a shear horizon with constant density (Chapter 3).

1.2 Perturbations

The interfaces of the shear horizon are subjected to a sinusoidal perturbation η around their initial position:

$$\begin{aligned} \eta^+(x,t) &= \widehat{\eta^+}.e^{i(kx-wt)} \text{ around } z = d \\ \eta^-(x,t) &= \widehat{\eta^-}.e^{i(kx-wt)} \text{ around } z = -d \end{aligned} \qquad (2)$$

With $\widehat{\eta^+}$ and $\widehat{\eta^-}$ the amplitudes of the perturbations.

It follows that the velocity $\boldsymbol{U}$, the fluid pressure P, and the fluid density ρ will deviate from their initial state, the resulting variables being written as the sum of the initial field $(\overline{\boldsymbol{U}}, \bar{\rho}, \bar{P})$ and perturbations $(\boldsymbol{u}', \rho', p')$:

$$\begin{aligned} \boldsymbol{U} &= \overline{\boldsymbol{U}} + \boldsymbol{u}' \\ \rho &= \bar{\rho} + \rho' \qquad (3) \\ P &= \bar{P} + p' \end{aligned}$$

With $\boldsymbol{U}(x,z,t) = \binom{U_x\,(x,z,t)}{U_z(x,z,t)}$, $\overline{\boldsymbol{U}} = \binom{\overline{U_x(z)}}{0}$ and $\boldsymbol{u}' = \binom{u_x{}'(x,z,t)}{u_z{}'(x,z,t)}$.

1.4 Constitutive equations

(1) The conservation of momentum for an inviscid fluid solely driven by gravity is:

$$\begin{aligned} \frac{d\rho\boldsymbol{U}}{dt} &= \rho.\frac{d\boldsymbol{U}}{dt} + \boldsymbol{U}.\frac{d\rho}{dt} \\ \frac{d\rho\boldsymbol{U}}{dt} &= \rho.\vec{g} - \overrightarrow{grad}(P) \end{aligned} \qquad (4)$$

with $\vec{g} = \binom{0}{-g}$ the gravity acceleration.

(2) The mass conservation yields to the continuity equation:

$$\frac{\partial\rho}{\partial t} + div(\rho.\boldsymbol{U}) = 0 \qquad (5)$$

(3) The assumption of incompressibility entrains that the total derivative of the density (the variations following a volume of fluid) has to be zero. This means that density changes can be advected but not diffused, i.e:

$$\frac{D\rho}{Dt} = 0 \leftrightarrow \frac{\partial\rho}{\partial t} + \boldsymbol{U}.\overrightarrow{grad}(\rho) = 0 \; (6)$$

Finally, combining the incompressibility (6) and continuity equations (5) for a non-zero density yields:

$$Div(\boldsymbol{U}) = 0 \leftrightarrow \frac{\partial U_x}{\partial x} + \frac{\partial U_z}{\partial z} = 0 \; (7)$$

This expressions shows that the velocity can be written as deriving from a potential, yet this implies an irrotational flow.

1.5. Boundary conditions

In order to resolve the problem, several boundary conditions are involved.

1.5.1. Finite perturbations

The perturbation of the interfaces is considered as having a finite influence, so that its effect far away from the interfaces is vanishing. Concretely, this means that any effect should vanish with $z \Rightarrow \pm\infty$.

1.5.2. Continuity of the vertical velocity at the interfaces

-The fluid particles at the interfaces of the shear horizon in $z = d + \eta^+$ and $z = -d + \eta^-$ must move with the interfaces, avoiding collocations of two fluids at the same time, as well as cavitation formed between the fluids. This condition is translated into the following equations:

at $z = d + \eta^+$

$$\frac{D\eta^+}{Dt} = \frac{\partial \eta^+}{\partial t} + U_x(z = d^+ + \eta^+).\frac{\partial \eta^+}{\partial x} = U_z(z = d^+ + \eta^+)$$
$$\frac{D\eta^+}{Dt} = \frac{\partial \eta^+}{\partial t} + U_x(z = d^- + \eta^+).\frac{\partial \eta^+}{\partial x} = U_z(z = d^- + \eta^+) \quad (8)$$

at $z = -d + \eta^-$

$$\frac{D\eta^-}{Dt} = \frac{\partial \eta^-}{\partial t} + U_x(z = -d^+ + \eta^-).\frac{\partial \eta^-}{\partial x} = U_z(z = -d^+ + \eta^-)$$
$$\frac{D\eta^-}{Dt} = \frac{\partial \eta^-}{\partial t} + U_x(z = -d^- + \eta^-).\frac{\partial \eta^-}{\partial x} = U_z(z = -d^- + \eta) \quad (9)$$

1.5.3. Continuity of the pressure at the interfaces

At an interface with negligible thickness, the continuity principle states that the fluid pressure at both sides of the interface should be equal. As the initial pressure field is continuous, the perturbed term *p'* is continuous too:

$$p'(z = d^+ + \eta^+) = p'(z = d^- + \eta^+) \; and \; p'(z = -d^+ + \eta^-) = p'(z = -d^- + \eta^-) \quad (10)$$

With all these conditions, the problem is now fully posed in terms of physics, and can be resolved. In the following, we develop two examples of analytic mathematical resolutions. The first model considers two mediums of constant and similar density. The second one considers two flows with a linear density gradient decreasing with height. The shear horizon is considered as a mixing zone with an averaged and constant density.

1.6. Assumptions of small variations and small perturbations

Common assumptions are made on the quantities of the problem for linearization of constitutive equations:

(1). Oscillations of the interfaces only generate weak perturbations on the velocity field and its derivatives compared to the flow velocity, i.e.:

$$\boldsymbol{u}' \ll \boldsymbol{U}$$
$$\frac{\partial \boldsymbol{u}'}{\partial x} \ll \boldsymbol{U} \; and \; \frac{\partial \boldsymbol{u}'}{\partial z} \ll \boldsymbol{U} \quad and \quad \frac{\partial \boldsymbol{u}'}{\partial t} \ll \boldsymbol{U}$$

(2). Pressure fluctuations are weak compared to the pressure field:

$$p' \ll \bar{P}$$

(3*) Further, the Boussinesq approximation will be used for the case of a non-constant density (see chapter 4).

2. Resolution for two flows with constant density

In our first case, the density is considered as a constant value ρ_0 for the whole system.

A set of three equations now controls the evolution of the perturbed flow:

$$\frac{\partial U_x}{\partial t} + U_x.\frac{\partial U_x}{\partial x} + U_z.\frac{\partial U_x}{\partial z} = -\frac{1}{\rho_0}.\frac{\partial P}{\partial x}$$
$$\frac{\partial U_z}{\partial t} + U_x.\frac{\partial U_z}{\partial x} + U_z.\frac{\partial U_z}{\partial z} = -g - \frac{1}{\rho_0}.\frac{\partial P}{\partial z} \quad (11)$$
$$\frac{\partial U_x}{\partial x} + \frac{\partial U_z}{\partial z} = 0$$

Since the initial flow should obey the constitutive equations, and given that the vertical velocity of the initial flow is null, $\bar{U}$ is ruled by:

$$\frac{\partial \overline{U_x}}{\partial t}+\overline{U_x}.\frac{\partial \overline{U_x}}{\partial x}+\overline{U_z}.\frac{\partial \overline{U_x}}{\partial z}=-\frac{1}{\overline{\rho_0}}.\frac{\partial \bar{P}}{\partial x} \quad (12a)$$

$$g=-\frac{1}{\overline{\rho_0}}.\frac{\partial \bar{P}}{\partial z} \quad (12b)$$

$$\frac{\partial \overline{U_x}}{\partial x}=0 \quad (12c)$$

Equation (12c)is also a natural consequence of the initial problem being posed without an horizontal length scale.

Substituting the expression of the perturbed values into (11) and considering the first-order approximations (7, 8, 9), as well as using the equations of the initial flow (12), it results a set of perturbation equations with the following form:

$$\frac{\partial u_x{}'}{\partial t}+\overline{U_x}.\frac{\partial u_x{}'}{\partial x}+u_z'.\frac{\partial \overline{U_x}}{\partial z}=-\frac{1}{\rho_0}\frac{\partial p'}{\partial x} \quad (13a)$$

$$\frac{\partial u_{z'}}{\partial t}+\overline{U_x}.\frac{\partial u_{z'}}{\partial x}=-g-\frac{1}{\rho_0}\frac{\partial p'}{\partial z} \quad (13b)$$

$$\frac{\partial u_x{}'}{\partial x}+\frac{\partial u_z{}'}{\partial z}=0 \quad (13c)$$

2.1. Establishing the Rayleigh equation

Differentiating (13a) with respect to z and (13b) with respect to x yields:

$$\frac{\partial^2 u_x{}'}{\partial t\partial z}+\frac{\partial \overline{U_x}}{\partial z}.\frac{\partial u_x{}'}{\partial x}+\overline{U_x}.\frac{\partial^2 u_x{}'}{\partial x\partial z}+\frac{\partial u_z{}'}{\partial z}.\frac{\partial \overline{U_x}}{\partial z}+u_z'.\frac{\partial^2 \overline{U_x}}{\partial z^2}=-\frac{1}{\rho_0}\frac{\partial^2 p'}{\partial x\partial z} \quad (14a)$$

$$\frac{\partial^2 u_{z'}}{\partial t\partial x}+\frac{\partial \overline{U_x}}{\partial x}.\frac{\partial u_z{}'}{\partial x}+\overline{U_x}.\frac{\partial^2 u_{z'}}{\partial x^2}=-\frac{1}{\rho_0}\frac{\partial^2 p'}{\partial z\partial x} \quad (14b)$$

Adding (14a) and (14b) eliminates the pressure terms in an expression rewritten as:

$$\frac{\partial^2 u_x{}'}{\partial t\partial z}+\frac{\partial \overline{U_x}}{\partial z}.\frac{\partial u_x{}'}{\partial x}+\overline{U_x}.\frac{\partial^2 u_x{}'}{\partial x\partial z}+\frac{\partial u_z{}'}{\partial z}.\frac{\partial \overline{U_x}}{\partial z}+u_z'.\frac{\partial^2 \overline{U_x}}{\partial z^2}$$
$$=\frac{\partial^2 u_{z'}}{\partial t\partial x}+\frac{\partial \overline{U_x}}{\partial x}.\frac{\partial u_z{}'}{\partial x}+\overline{U_x}.\frac{\partial^2 u_{z'}}{\partial x^2} \quad (15)$$

The perturbed velocity satisfies the incompressibility equation (13c) so that we can define a stream function such as:

$$u_x'=\frac{\partial \varphi}{\partial z}$$
$$u_z'=-\frac{\partial \varphi}{\partial x} \quad (16)$$

with φ the perturbed potential associated with the velocity perturbation. Note that this implies that the flow is irrotational.

Introducing these expressions (16) into (15) yields:

$$\frac{\partial^3 \varphi}{\partial t\partial z^2}+\frac{\partial \overline{U_x}}{\partial z}.\frac{\partial^2 \varphi}{\partial x\partial z}+\overline{U_x}.\frac{\partial^3 \varphi}{\partial x\partial z^2}-\frac{\partial^2 \varphi}{\partial z\partial x}.\frac{\partial \overline{U_x}}{\partial z}-\frac{\partial \varphi}{\partial x}.\frac{\partial^2 \overline{U_x}}{\partial z^2}=\frac{\partial^3 \varphi}{\partial t\partial x^2}-\frac{\partial \overline{U_x}}{\partial x}.\frac{\partial^2 \varphi}{\partial x^2}-\overline{U_x}.\frac{\partial^3 \varphi}{\partial x^3} \quad (16)$$

This expression shows that φ and p' are solutions of coupled equations with coefficients only involving the z coordinate. Solutions for such equations are normal modes in the form:

$$\varphi=\hat{\varphi}.e^{i(kx-wt)}$$
$$p'=\widehat{p'}.e^{i(kx-wt)} \quad (17)$$

where $\hat{\varphi}$ and $\widehat{p'}$ are the z-dependent amplitudes of perturbations on the velocity potential and the fluid pressure, respectively.

The wave velocity is defined as:

$$c=\frac{w}{k} \quad (18)$$

Using (18) and substituting (17) into (16) yields, after division by $i.k$:

$$k^2.c.\hat{\varphi}-c\frac{\partial^2 \hat{\varphi}}{\partial z^2}-\overline{U_x}.k^2.\hat{\varphi}+\overline{U_x}.\frac{\partial^2 \hat{\varphi}}{\partial z^2}-\frac{\partial^2 \overline{U_x}}{\partial z^2}.\hat{\varphi}=0 \quad (19)$$

Rearranging the terms and dividing by $(\frac{1}{(\overline{U_x}-c)})$ yields the Rayleigh equation:

$$\frac{d^2\hat{\varphi}}{dz^2}-\left[\frac{1}{(\overline{U_x}-c)}.\frac{d^2\overline{U_x}}{dz^2}+k^2\right].\hat{\varphi}=0 \quad (20)$$

2.2. Resolution of the Rayleigh equation for the perturbed flow

2.2.1. The specific case of piecewise linear profiles of fluid velocity

Usually, the resolution of the Rayleigh equation is complicated, but the geometry of the problem with piecewise linear profiles of velocity and density enables to find an analytical solution. The initial flow is linear apart at shear interfaces, i.e.:

$$\frac{d^2\overline{U_x}}{dz^2} = 0 \; for \; |z| < d \; and \; for \; |z| > d$$

Within the three domains, the Taylor-Goldstein equation simplifies into an ordinary second-order differential equation:

$$\frac{d^2\hat{\varphi}}{dz^2} - k^2.\hat{\varphi} = 0 \qquad (21)$$

With a well-established solution given by:

$$\hat{\varphi} = \begin{cases} B_+.e^{-kz} \; for \; z > d \\ A_-.e^{kz} for \; z < -d \\ A.e^{kz} + B.e^{-kz} \; for \; |z| < d \end{cases} \qquad (22)$$

Note that we omitted the increasing exponentials of the general solution because the perturbation should vanish away from the interfaces (boundary condition 1.5.1).

2.2.2. Continuity of the vertical velocity at the interfaces

In order to find the dispersion equation of the pulsation *w* as a function of k, the constants (B_+, A, B, A_-) must be constrained. Recall the property of the continuity of the normal velocity at the interfaces $z = d + \eta^+$ and $z = -d + \eta^-$ (boundary condition 1.5.2).

By substituting the expressions of U_x, U_z, η^+, η^- and $u_z{}'$ and neglecting the second-order terms, a linearized system is obtained:

at $z = d + \eta^+$

$$\begin{aligned} -c.\eta^+ + U_0.\eta^+ &= B^+.e^{-\alpha d} \\ -c.\eta^+ + U_0.\eta^+ &= A.e^{kd} + B.e^{-kd} \end{aligned} \qquad (23a)$$

at $z = -d + \eta^-$

$$\begin{aligned} -c.\eta^- + U_0.\eta^- &= A.e^{-kd} + B.e^{kd} \\ -c.\eta^+ + U_0.\eta^+ &= A^-.e^{-\alpha d} \end{aligned} \qquad (23b)$$

And by combining side by side equations (23a) and (23b), two relationships between the constants (B_+, A, B, A_-) are obtained:

$$\begin{aligned} B^+ &= \left(A.e^{kd} + B.e^{-kd}\right).e^{\alpha d} \\ A^- &= \left(A.e^{-kd} + B.e^{kd}\right).e^{-\alpha d} \end{aligned} \qquad (24)$$

So that (22) becomes:

$$\hat{\varphi} = \begin{cases} \left(A.e^{kd} + B.e^{-kd}\right).e^{\alpha d}.e^{-\alpha z} \; for \; z > d \\ \left(A.e^{-kd} + B.e^{kd}\right).e^{-\alpha d}.e^{\alpha z} \quad for \; z < -d \\ A.e^{kz} + B.e^{-kz} \qquad for \; |z| < d \end{cases} \qquad (25)$$

2.2.3. Continuity of the pressure at the interfaces

A relationship between $\hat{\varphi}$ and $\widehat{p'}$ is established by introducing the expressions of p', $u_1{}'$ and $u_2{}'$ into the Momentum equation (11):

$$(\overline{U_x} - c).\frac{\partial\hat{\varphi}}{\partial z} - \frac{\partial\overline{U_x}}{\partial z}.\hat{\varphi} = \frac{1}{\rho_0}.\widehat{p'} \qquad (26)$$

Given that pressure shall be continuous at the interface (boundary condition 1.5.3), it follows from (26) that the quantity $(\overline{U_x} - c).\frac{\partial\hat{\varphi}}{\partial z} - \frac{\partial\overline{U_x}}{\partial z}.\hat{\varphi}$ also varies continuously at the interfaces. By replacing $\overline{U_x}$ by its expression, the conditions at the interfaces appear as:

- at $z = d + \eta^+$:

$$(U_0 - c).\left.\frac{\partial\hat{\varphi}}{\partial z}\right|_{d^+ + \eta^+} + 0.\hat{\varphi}|_{d^+ + \eta^+} = (U_0 - c).\left.\frac{\partial\hat{\varphi}}{\partial z}\right|_{d^- + \eta^+} - \frac{U_0}{d}.\hat{\varphi}_{d^- + \eta^+} \qquad (27a)$$

- at $z = -d + \eta^-$:

$$(-U_0-c).\frac{\partial\hat{\varphi}}{\partial z}\Big|_{-d^{+}+\eta^{-}}-\frac{U_0}{d}.\hat{\varphi}|_{-d^{+}+\eta^{-}}=(-U_0-c).\frac{\partial\hat{\varphi}}{\partial z}\Big|_{-d^{-}+\eta^{-}}-0.\hat{\varphi}|_{-d^{-}+\eta^{-}} \quad (27b)$$

Introducing the expression of $\hat{\varphi}$ given by (25) into (27a) and (27b) gives a new relationship between the constants A and B:

- At $z=d+\eta^{+}$:

$$k.(c-U_0).\left(A.e^{kd}+B.e^{-kd}\right)=k.(U_0-c).\left(A.e^{kd}-B.e^{-kd}\right)-\frac{U_0}{d}.\left(A.e^{kd}+B.e^{-kd}\right) \quad (28a)$$

- At $z=-d+\eta^{-}$:

$$-k.(U_0+c).\left(A.e^{-kd}-B.e^{kd}\right)-\frac{U_0}{d}.\left(A.e^{-kd}+B.e^{kd}\right)$$
$$=-k.(U_0+c).\left(A.e^{-kd}+B.e^{kd}\right) \quad (28b)$$

Rearranging the terms of (28a) and (27a) yields the system:

$$\begin{aligned}\left[2k(c-U_0)+\frac{U_0}{d}\right].A+\left[\frac{U_0}{d}.e^{-2kd}\right].B&=0\\ \left[-\frac{U_0}{d}.e^{-2kd}\right].A+\left[2k(U_0+c)-\frac{U_0}{d}\right].B&=0\end{aligned} \quad (29)$$

2.3. Finding the dispersion equation for the perturbation

The previous system has a non-trivial solution if the determinant of system (29) is 0, i.e.:

$$\left[2k(c-U_0)+\frac{U_0}{d}\right].\left[2k(U_0+c)-\frac{U_0}{d}\right]-\left[\frac{U_0}{d}.e^{-2kd}\right].\left[-\frac{U_0}{d}.e^{-2kd}\right]=0 \quad (30)$$

With some rearrangements, (30) is equivalent to:

$$\boxed{4w^2-4k^2U_0^2+4k\frac{U_0^2}{d}-\frac{U_0^2}{d^2}+\frac{U_0^2}{d^2}.e^{-4kd}=0 \quad (31)}$$

It corresponds to the dispersion equation for the perturbation: if w is real then the perturbation is a periodic wave, otherwise the perturbation is unstable and its growth rate is given by the imaginary part of w. The roots of this complex equation are found numerically using the Matlab solver “solve” (Fig 13).

3. Case of flows with a linear density gradient

We now consider the case of two flows with a linear density gradient. The shear horizon is considered as a mixing zone with an averaged and constant. The resolution of the dispersed equation follows a similar structure and method as for the constant density.

The initial density profile is defined by:

$$\frac{d\overline{\rho(z)}}{dz}=\begin{cases} s \ if \ z>d\\ s \ if \ z<-d\\ 0 \ if \ |z|<d\end{cases} \quad (32)$$

And the perturbation of the interface entrains perturbation such as:

$$\rho\,(x,z,t)=\bar{\rho}(z)+\rho'(x,z,t) \ (33)$$

3.1. Linearization

For the case of varying density, the often used Boussinesq approximation is introduced. This approximation considers that the density ρ is the sum of a mean density ρ_0 and a varying term ρ'' that is weak and weakly evolving compared to ρ_0 and the velocity fluctuations:

$$\begin{gathered}\rho(x,z,t)=\rho_0+\rho''(x,z,t) \ with \ \rho''\ll\rho_0\\ \frac{d\rho}{dt}=\frac{d\rho''}{dt}\ll\frac{d\boldsymbol{U}}{dt}\end{gathered} \quad (34)$$

It results that we ignore the products of ρ'' with small quantities, as well as any derivative of ρ'' so that, (9a) simplifies into:

$$\frac{d\rho\boldsymbol{U}}{dt}=(\rho_0+\rho'').\frac{d\boldsymbol{U}}{dt}+U.\frac{d\rho''}{dt}\cong\rho_0.\frac{d\boldsymbol{U}}{dt} \ (35)$$

Thus, equalizing (10) and (9b) and developing $\frac{d\boldsymbol{U}}{dt}$ yields:

$$\rho_0.\left[\frac{\partial\boldsymbol{U}}{\partial t}+\left(\boldsymbol{U}.\overrightarrow{\mathrm{grad}}\right).\boldsymbol{U}\right]=\rho.\vec{\boldsymbol{g}}-\overrightarrow{grad}(P) \quad (36)$$

so that density fluctuations in (36) are only accounted for in the buoyancy $\rho.\vec{\boldsymbol{g}}$, all other occurrences of ρ being approximated as ρ_0.
Since the initial flow should obey this modified equation of momentum (36), $\overline{\boldsymbol{U}}$ in (1) and $\bar{\rho}$ in (32) shall satisfy on both space directions:

$$\begin{aligned}\frac{\partial\overline{U_x}}{\partial t}+\overline{U_x}.\frac{\partial\overline{U_x}}{\partial x}+\overline{U_z}.\frac{\partial\overline{U_x}}{\partial z}&=-\frac{1}{\rho_0}.\frac{\partial\bar{P}}{\partial x}\\ \frac{\partial\overline{U_z}}{\partial t}+\overline{U_x}.\frac{\partial\overline{U_z}}{\partial x}+\overline{U_z}.\frac{\partial\overline{U_z}}{\partial z}+\frac{\bar{\rho}}{\rho_0}.g&=-\frac{1}{\rho_0}.\frac{\partial\bar{P}}{\partial z}\end{aligned}\qquad(37)$$

Similarly, the initial flow is incompressible (7) and the vertical velocity of the initial flow is null, so that:

$$\frac{\partial\overline{U_x}}{\partial x}=0\qquad(38)$$

This latter equality is also a natural consequence of the initial problem being posed without horizontal length scale.
A set of four equations now controls the evolution of the perturbed flow:

$$\begin{aligned}\frac{\partial U_x}{\partial t}+U_x.\frac{\partial U_x}{\partial x}+U_z.\frac{\partial U_x}{\partial z}&=-\frac{1}{\rho_0}.\frac{\partial P}{\partial x}\\ \frac{\partial U_z}{\partial t}+U_x.\frac{\partial U_z}{\partial x}+U_z.\frac{\partial U_z}{\partial z}&=-\frac{\rho}{\rho_0}.g-\frac{1}{\rho_0}.\frac{\partial P}{\partial z}\\ \frac{\partial\rho}{\partial t}+div(\rho.\boldsymbol{U})&=0\\ \frac{\partial U_x}{\partial x}+\frac{\partial U_z}{\partial z}&=0\end{aligned}\qquad(39)$$

Substituting the expressions of the perturbed state into (39), and simplifying with the first order approximations, removing terms that are zero by definition, and using the relations on the initial flow (37 and 38), the system translates as:

$$\frac{\partial u_x{}'}{\partial t}+\overline{U_x}.\frac{\partial u_x{}'}{\partial x}+u_z'.\frac{\partial\overline{U_x}}{\partial z}=-\frac{1}{\rho_0}\frac{\partial p'}{\partial x}\qquad(40a)$$

$$\frac{\partial u_{z'}}{\partial t}+\overline{U_x}.\frac{\partial u_{z'}}{\partial x}=-\frac{\rho'}{\rho_0}.g-\frac{1}{\rho_0}\frac{\partial p'}{\partial z}\qquad(40b)$$

$$\frac{\partial\rho'}{\partial t}+\bar{\rho}.\frac{\partial u_x{}'}{\partial t}+\overline{U_x}.\frac{\partial\rho'}{\partial x}+u_z'.\frac{\partial\bar{\rho}}{\partial z}+\bar{\rho}.\frac{\partial u_z{}'}{\partial z}=0\qquad(40c)$$

$$\frac{\partial u_x{}'}{\partial x}+\frac{\partial u_z{}'}{\partial z}=0\qquad(40d)$$

3.2. Establishing the Taylor Goldstein equation
Differentiating (40a) with respect to *z* and (40b) with respect to *x* yields:

$$\frac{\partial^2 u_x{}'}{\partial t\partial z}+\frac{\partial\overline{U_x}}{\partial z}.\frac{\partial u_x{}'}{\partial x}+\overline{U_x}.\frac{\partial^2 u_x{}'}{\partial x\partial z}+\frac{\partial u_z{}'}{\partial z}.\frac{\partial\overline{U_x}}{\partial z}+u_z'.\frac{\partial^2\overline{U_x}}{\partial z^2}=-\frac{1}{\rho_0}\frac{\partial^2 p'}{\partial x\partial z}\qquad(41a)$$

$$\frac{\partial^2 u_{z'}}{\partial t\partial x}+\overline{U_x}.\frac{\partial^2 u_{z'}}{\partial x^2}-\frac{g}{\rho_0}.\frac{\partial\rho'}{\partial x}=-\frac{1}{\rho_0}\frac{\partial^2 p'}{\partial z\partial x}\qquad(41b)$$

Adding (41a) and (41b) eliminates the pressure terms in an expression rewritten as:

$$\frac{\partial^2 u_x{}'}{\partial t\partial z}+\frac{\partial\overline{U_x}}{\partial z}.\frac{\partial u_x{}'}{\partial x}+\overline{U_x}.\frac{\partial^2 u_x{}'}{\partial x\partial z}+\frac{\partial u_z{}'}{\partial z}.\frac{\partial\overline{U_x}}{\partial z}+u_z'.\frac{\partial^2\overline{U_x}}{\partial z^2}=\frac{\partial^2 u_{z'}}{\partial t\partial x}+\overline{U_x}.\frac{\partial^2 u_{z'}}{\partial x^2}-\frac{g}{\rho_0}.\frac{\partial\rho'}{\partial x}\qquad(42)$$

A stream function is defined for the perturbation, which satisfies the incompressibility equation (40d):

$$\begin{aligned}u_x'&=\frac{\partial\varphi}{\partial z}\\ u_z'&=-\frac{\partial\varphi}{\partial x}\end{aligned}\qquad(43)$$

with φ the perturbed potential associated to the velocity perturbation.
Introducing the stream function (43) into (42) yields:

$$\frac{\partial^3\varphi}{\partial t\partial z^2}+\frac{\partial\overline{U_x}}{\partial z}.\frac{\partial^2\varphi}{\partial x\partial z}+\overline{U_x}.\frac{\partial^3\varphi}{\partial x\partial z^2}-\frac{\partial^2\varphi}{\partial z\partial x}.\frac{\partial\overline{U_x}}{\partial z}-\frac{\partial\varphi}{\partial x}.\frac{\partial^2\overline{U_x}}{\partial z^2}=-\frac{\partial^3\varphi}{\partial t\partial x^2}-\overline{U_x}.\frac{\partial^3\varphi}{\partial x^3}-\frac{g}{\rho_0}.\frac{\partial\rho'}{\partial x}\qquad(44)$$

ρ' and p' are thus solutions of coupled equations with coefficients only involving the z coordinate.
Solutions of such systems are normal modes of the form:

$$\varphi = \hat{\varphi}(z).e^{i(kx-wt)}$$
$$\rho' = \widehat{\rho'}(z).e^{i(kx-wt)} \qquad (45)$$
$$p' = \widehat{p'}(z).e^{i(kx-wt)}$$

where $\hat{\varphi}$, $\widehat{\rho'}$, and $\widehat{p'}$ are the amplitudes of perturbations on the potential, fluid density, and fluid pressure, respectively.
The wave velocity is defined as:

$$c = \frac{w}{k} \qquad (46)$$

Substituting (45) into (44) and using (46) yields:

$$k^2.c.\hat{\varphi} - c.\frac{\partial^2\hat{\varphi}}{\partial z^2} - \overline{U_x}.k^2.\hat{\varphi} + \overline{U_x}.\frac{\partial^2\hat{\varphi}}{\partial z^2} - \frac{\partial^2\overline{U_x}}{\partial z^2}.\hat{\varphi} = \frac{g}{\rho_0}.\widehat{\rho'} \qquad (47)$$

Similarly, replacing the expressions of (45) in (40c) allow to identify $\widehat{\rho'}$ as a function of $\hat{\varphi}$ and of the initial flow density profile $\frac{\partial\bar{\rho}}{\partial z}$:

$$(\overline{U_x} - c).\widehat{\rho'} = -\hat{\varphi}.\frac{\partial\bar{\rho}}{\partial z} \qquad (48)$$

Combining (48) and (46) results in the Taylor-Goldstein equation:

$$\boxed{\frac{\partial^2\hat{\varphi}}{\partial z^2} + \left[\frac{N^2}{(\overline{U_x} - c)^2} - \frac{1}{\overline{U_x} - c}.\frac{\partial^2\overline{U_x}}{\partial z^2} - k^2\right].\hat{\varphi} = 0 \qquad (49a)}$$

With N^2 the buoyancy frequency (or Brunt-Väisälä frequency) defined as:

$$N^2 = -\frac{g}{\rho_0}.\frac{d\bar{\rho}}{dz} \qquad (49b)$$

N^2 is a value describing the degree of stratification of the medium: fluids with strong vertical density gradient will be characterized by a high value of N^2.

3.3. Resolution of the Taylor-Goldstein equation for the initial flow

3.3.1. Piecewise linear profiles of density and velocity

As for the Rayleigh equation, the resolution of the Taylor-Goldstein equation is usually complicated but tackled analytically here via the piecewise linear profiles of velocity and density. The medium is split again so that:

$$\begin{matrix}\frac{\partial^2\overline{U_x}}{\partial z^2} = 0 \\ N^2 = 0\end{matrix} \quad \text{for } |z| < d \quad (50a)$$

and

$$\begin{matrix}\frac{\partial^2\overline{U_x}}{\partial z^2} = 0 \\ N^2 = N_0 = constant\end{matrix} \quad \text{for } |z| > d \quad (50b)$$

Within both domains, the Taylor-Goldstein equation simplifies to the following ordinary second-order differential equation:

$$\frac{d^2\hat{\varphi}}{dz^2} + \alpha^2.\hat{\varphi} = 0 \qquad (51a)$$

with:

$$\alpha^2 = \begin{cases} -k^2 \ for\ |z| < d \\ \frac{{N_0}^2}{(\overline{U_x} - c)^2}\ for\ |z| > d \end{cases} \qquad (51b)$$

The solution to such an ordinary differential equation (51a, 51b) is of the form:

$$\hat{\varphi} = \begin{cases} B_+.e^{-\alpha z}\ for\ z > d \\ A_-.e^{\alpha z} for\ z < -d \\ A.e^{kz} + B.e^{-kz}\ for\ |z| < d \end{cases} \qquad (52)$$

Again, the constant involving the exponential increasing for $z => \pm\infty$ are omitted because the perturbation is finite (boundary condition 1.5.1.).

In order to find the dispersion equation of the wave number w as a function of k, the constants (B_+, A, B, A_-) are again constrained through the boundary conditions of the normal velocity and pressure at the interfaces $z = d + \eta^+$ and $z = -d + \eta^-$.

3.3.2. Continuity of the vertical velocity at the interfaces

The fluid particles at the interfaces move with the interfaces (boundary condition 1.5.2.).

Introducing $U_x = \overline{U_x} + u_x'$ and $U_z = \overline{U_z} + u_z'$ for this condition, and neglecting the second-order terms, we obtain the following linearized system:

at $z = d + \eta^+$

$$\frac{\partial \eta^+}{\partial t} + U_0.\frac{\partial \eta^+}{\partial x} = u_z'(z = d^+ + \eta^+)$$
$$\frac{\partial \eta^+}{\partial t} + U_0.\frac{\partial \eta^+}{\partial x} = u_z'(z = d^- + \eta^+) \qquad (53a)$$

at $z = -d + \eta^-$

$$\frac{\partial \eta^-}{\partial t} - U_0.\frac{\partial \eta^-}{\partial x} = u_z'(z = -d^+ + \eta^-)$$
$$\frac{\partial \eta^-}{\partial t} - U_0.\frac{\partial \eta^-}{\partial x} = u_z'(z = -d^- + \eta^-) \qquad (53b)$$

Substituting the expressions of η^+, η^- and u_z' in (53a) and (53b) yields:

at $z = d + \eta^+$

$$-c.\eta^+ + U_0.\eta^+ = B^+.e^{-\alpha d}$$
$$-c.\eta^+ + U_0.\eta^+ = A.e^{kd} + B.e^{-kd} \qquad (54a)$$

- at $z = -d + \eta^-$

$$-c.\eta^- + U_0.\eta^- = A.e^{-kd} + B.e^{kd}$$
$$-c.\eta^+ + U_0.\eta^+ = A^-.e^{-\alpha d} \qquad (54b)$$

Therefore, adding side by side (54a) and (54b) gives two relationships between the constants:

$$B^+ = \left(A.e^{kd} + B.e^{-kd}\right).e^{\alpha d}$$
$$A^- = (A.e^{-kd} + B.e^{kd}).e^{-\alpha d} \qquad (55)$$

Thus (38) becomes:

Comment [gad1]: check

$$\hat{\varphi} = \begin{cases} \left(A.e^{kd} + B.e^{-kd}\right).e^{\alpha d}.e^{-\alpha z}\ for\ z > d \\ \left(A.e^{-kd} + B.e^{kd}\right).e^{-\alpha d}.e^{\alpha z}\ for\ z < -d \\ A.e^{kz} + B.e^{-kz} \qquad for\ |z| < d \end{cases} \qquad (56)$$

3.3.3. Continuity of the pressure at the interfaces

The relationship between $\hat{\varphi}$ and $\widehat{p'}$ is established by introducing the expressions of p', u_x' and u_z' into the momentum equation (24a) yields:

Comment [gad2]: check

$$(\overline{U_x} - c).\frac{\partial \hat{\varphi}}{\partial z} - \frac{\partial \overline{U_x}}{\partial z}.\hat{\varphi} = \frac{1}{\rho_0}.\widehat{p'} \qquad (57)$$

Using the continuity of pressure (boundary condition 1.5.3.), it comes that the quantity $(\overline{U_x} - c).\frac{\partial}{\partial z} - \frac{\partial \overline{U_x}}{\partial z}.\hat{\varphi}$ varies continuously at the interfaces $z = d + \eta^+$ and $z = -d + \eta^-$. Replacing $\overline{U_x}$ by its expression transforms the conditions at the interfaces in:

at $z = d + \eta^+$:

$$(U_0 - c).\frac{\partial \hat{\varphi}}{\partial z}\bigg|_{d^+ + \eta^+} + 0.\hat{\varphi}|_{d^+ + \eta^+} = (U_0 - c).\frac{\partial \hat{\varphi}}{\partial z}\bigg|_{d^- + \eta^+} - \frac{U_0}{d}.\hat{\varphi}_{d^- + \eta^+} \qquad (58a)$$

at $z = -d + \eta^-$:

$$(-U_0 - c).\frac{\partial \hat{\varphi}}{\partial z}\bigg|_{-d^+ + \eta^-} - \frac{U_0}{d}.\hat{\varphi}|_{-d^+ + \eta^-} = (-U_0 - c).\frac{\partial \hat{\varphi}}{\partial z}\bigg|_{-d^- + \eta^-} - 0.\hat{\varphi}|_{-d^- +} \qquad (58b)$$

Introducing the expression of $\hat{\varphi}$ given by (46) into (49) and (50) gives a new relationship between the constants A and B:

$$\alpha.(c - U_0).\left(A.e^{kd} + B.e^{-kd}\right) = k.(U_0 - c).\left(A.e^{kd} + B.e^{-kd}\right) - \frac{U_0}{d}.\left(A.e^{kd} + B.e^{-kd}\right)$$
$$-k.(U_0 + c).(A.e^{-kd} + B.e^{kd}) - \frac{U_0}{d}.(A.e^{-kd} + B.e^{kd}) = \alpha.(U_0 + c).(A.e^{-kd} + B.e^{kd}) \qquad (59)$$

3.3.4. Finding the dispersion equation for the perturbation

System (59) has a non-trivial solution if the determinant of the system is 0, i.e.:

$$w^3 + \frac{w^2}{2}.\left(1 + Ri.e^{2kd}\right) + \frac{w}{2}.Ri.\left(e^{2kd} - 1\right) + \frac{Ri}{2}.sinh^2(k.d) = 0$$
$$with\ Ri = \frac{{N_0}^2.d^2}{{U_0}^2}\ the\ bulk\ Richardson\ number \qquad (60)$$

The bulk Richardson number Ri is a ratio of the buoyancy over the shear forces and it thus quantifies the degree of stratification whereas the non-dimensional ratio $k.d$ quantifies the ratio between the wavelength of the perturbation and the thickness of the shear horizon.

System (60) corresponds to the dispersion equation for the perturbation: if w is real, the perturbation is a periodic wave, otherwise the perturbation is unstable and its growth rate is given by the imaginary part of w.